

A 3D WAVELET-BASED INCOMPRESSIBLE NAVIER-STOKES SOLVER FOR FULLY ADAPTIVE COMPUTATIONS IN TIME-VARYING GEOMETRIES *

THOMAS ENGELS^{*†‡§}, KAI SCHNEIDER[†], JULIUS REISS[§] AND MARIE FARGE[†]

Abstract. We present a wavelet-based adaptive method for computing 3D flows in complex, time-dependent geometries, implemented on massively parallel computers. The incompressible fluid is modeled with an artificial compressibility approach in order to avoid the solution of elliptical problems. No-slip and in/outflow boundary conditions are imposed using volume penalization. The governing equations are discretized on a locally uniform Cartesian grid with centered finite differences, and integrated in time with a Runge-Kutta scheme, both of 4th order. The domain is partitioned into cubic blocks with equidistant grids and, for each block, biorthogonal interpolating wavelets are used as refinement indicators and prediction operators. Thresholding of wavelet coefficients allows to introduce dynamically evolving grids and the adaption strategy tracks the solution in both space and scale. Blocks are distributed among MPI processes and the global topology of the grid is encoded in a tree-like data structure. Analyzing the different physical and numerical parameters allows balancing their individual error contributions and thus ensures optimal convergence while minimizing computational effort. Different validation tests score accuracy and performance of our new open source code, **WABBIT** (Wavelet Adaptive Block-Based solver for Interactions with Turbulence), on massively parallel computers using fully adaptive grids. Flow simulations of flapping insects demonstrate its applicability to complex, bio-inspired problems. (<https://github.com/adaptive-cfd/WABBIT>).

Key words. adaptive numerical method, wavelets, volume penalization, artificial compressibility, flapping flight

AMS subject classifications. 65M06; 65M50; 65M55; 65M85; 65T60; 76M20; 76D05; 76Z10

1. Introduction. Computing flows in complex geometries, which may move or deform, is required for multiple applications, *e.g.*, many biological flow problems like flying insects or beating hearts. In particular in the turbulent flow regime this is still a major challenge for computational fluid dynamics. Turbulence and moving boundaries require numerical techniques that can track the solution in space and scale to dynamically adapt the numerical grid accordingly, especially in cases where fluid-structure interaction is considered, since the motion of the boundary is then not known *a priori*, but rather depends on the nonlinear interaction with the fluid. In this regard adaptive numerical discretization methods, which can be traced back to the 1980s [7, 6], are indeed attractive. In many cases they can be much more competitive than schemes on regular fine grids, depending on the character of the solution. However, for adaptive discretizations two major challenges can be identified:

*Corresponding author, e-mail address: thomas.engels@ens.fr

[†]LMD UMR 8539 'ECOLE NORMALE SUPÉRIEURE-PSL, PARIS, FRANCE

[‡]AIX-MARSEILLE UNIVERSITÉ, CNRS, I2M UMR 7373, MARSEILLE, FRANCE

[§]ISTA, TECHNISCHE UNIVERSITÄT BERLIN, BERLIN, GERMANY

*Submitted to the editors 11 December 2019.

Funding: TE, KS, MF gratefully acknowledge financial support from the Agence Nationale de la Recherche (ANR), Grant No. 15-CE40-0019, and Deutsche Forschungsgemeinschaft (DFG), Grant No. SE 824/26-1, project AIFIT. The authors were granted access to the HPC resources of IDRIS under the Allocation No. 2018-91664 attributed by GENCI (Grand Équipement National de Calcul Intensif). For this work, we were also granted access to the HPC resources of Aix-Marseille Université financed by the project Equip@Meso (No. ANR-10-EQPX-29-01). The authors thankfully acknowledge financial support granted by the ministères des Affaires étrangères et du développement international (MAEDI) et de l'Education nationale et l'enseignement supérieur, de la recherche et de l'innovation (MENESRI), and the Deutscher Akademischer Austauschdienst (DAAD) within the French-German Procope project FIFIT. JR, TE gratefully acknowledge financial support from the DFG SFB1029.

their actual implementation on massively parallel computers and the numerical error analysis of adaptivity.

The implementation of the code is crucial to optimize computing and two conceptually different approaches can be distinguished: one uses point-based techniques, while the other uses block-based techniques. In the former, the error indicator determines for each grid point whether it is significant or not (*e.g.*, [59, 45]), while for the latter significant grid points are clustered in patches with the drawback of including non-significant points and thus decreasing the compression rate [24]. Due to the hardware layout of modern CPUs, block-based implementations are in many cases more competitive and have become increasingly popular during the last years, see, *e.g.*, [63] for a recent review on available software packages. The locally regular block data can be transferred in one contiguous chunk to the CPU cache, which greatly increases the performance despite an increase in number of points.

The mathematical support for adaptivity needs to provide reliable error estimators of the solution and, for evolutionary problems, a prediction of the grid for the next time step. For both, a variety of heuristic criteria exists, *e.g.*, gradient-based approaches [18]. Adaptive mesh refinement algorithms use these heuristic criteria and are *error-indicated* methods because of their heuristic nature. *A-posteriori* error estimators [4] are mathematically rigorous but require solving expensive adjoint problems.

Wavelets and related multiresolution analysis techniques provide likewise a mathematical framework and yield reliable error estimators, coupled with high computational efficiency, and are thus well suited for developing adaptive solvers with *error control*. The idea of wavelet analysis is to decompose data into space and scale (and possibly directional) contributions. The wavelet transform has been introduced by Grossmann and Morlet [37], and the algorithm of the fast wavelet transform by Mallat [50]. Nonlinear approximation [21] provides the conceptual support for adaptivity; indeed, it introduces a systematic way to classify functions according to the sparsity of their representation in wavelet space, *i.e.*, the possibility of describing a function by a small number of wavelet coefficients. Wavelet-based algorithms for solving PDEs, starting with [49], were the first ones to be proved to guarantee the best n -term approximation [11]. The books of Cohen [10] and Müller [53] and the review articles [23, 62] give a detailed overview on the subject.

To take into account boundary conditions for complex geometries, in particular at solid walls, the family of immersed boundary methods (IBM) [57, 52, 61] is now often preferred over the traditional body-fitted grids for complex geometries. While the latter can yield better accuracy near the wall, IBM approaches convince with their ease of implementation and great flexibility. An early application for computing flow in a beating heart can be found in [56], illustrating that this class of methods has been designed from the start for complex, bio-inspired flow problems. Among the variety of methods, the volume penalization method [3], physically motivated by flow in porous media, is furthermore distinguished by its convergence proof for nonlinear Navier–Stokes [2]. Moreover its convergence properties are improved in the turbulent regime [54].

In biological applications the flow can be typically described as incompressible, which requires specialized numerical techniques to decouple the pressure from the velocity, most of which involve solving a Poisson equation. While there are adaptive solvers following this strategy, *e.g.*, [45], alternative methods such as the Lattice–Boltzmann method are an attractive choice for adaptive simulations due to their explicit character [63]. Another recently revisited method [55] is the artificial com-

compressibility method [9], which introduces a large but finite speed of sound and avoids solving elliptic equations.

In this work, we present a wavelet-based fully adaptive approach for solving the incompressible Navier–Stokes equations in complex and time-varying geometries on massively parallel computers. To this end we combine two physically motivated models: the artificial compressibility approach, to relax the kinematic incompressibility constraint and to allow for a finite speed of sound, and the volume penalization, which models solid objects as porous media with finite permeability. In the limit when the speed of sound and the permeability parameters tend to infinity and to zero, respectively, we recover the incompressible Navier–Stokes equations with no-slip boundary conditions. The numerical method for solving the resulting model equations is based on centered finite differences and explicit time integration, both of 4th order. The MPI parallel implementation uses block-based grids, which are coarsened and refined using biorthogonal wavelets. While the framework we present is quite general and can be applied to a large variety of fields, our main motivation for its development comes from the spectacular flight capabilities of flying insects, which use flapping wings to create the required aerodynamic forces.

The remainder of the paper presents the governing equations (sec. 2) followed by the numerical method including discretization errors (sec. 3) and the multiresolution analysis for introducing adaptivity (sec. 4). The choice of the parameters for balancing the different errors is discussed in sec. 5. The parallel implementation is presented in sec. 6. Different numerical results are shown in sec. 7 and the performance of the code is analyzed in sec. 8. Finally, conclusions are drawn in sec. 9.

2. Governing equations and modeling errors.

2.1. Artificial compressibility. The applications we have in mind involve exterior, incompressible flows past obstacles of complex shape which may vary in time. Numerical methods for such flows usually require the solution of a Poisson-type, elliptic PDE. Even though powerful libraries (*e.g.*, PETSc [1]) exist for that purpose, the solution of the Poisson equation is causing major computational cost, especially on irregular, time-dependent grids.

Instead of the incompressible Navier–Stokes equations,

$$(2.1) \quad \partial_t \underline{u} + (\underline{u} \cdot \nabla) \underline{u} + \nabla p - \nu \nabla^2 \underline{u} = 0$$

$$(2.2) \quad \nabla \cdot \underline{u} = 0$$

for the velocity \underline{u} and the pressure p in the fluid domain $\Omega_f \subset \mathbb{R}^D$ for $t > 0$ and $D = 2$ or 3 , completed with suitable boundary and initial conditions, and where ν is the kinematic viscosity, we consider the artificial compressibility method (ACM). An artificial speed of sound $C_0 \gg |\underline{u}|$ is introduced and eqn. (2.2) is replaced by

$$(2.3) \quad \partial_t p + C_0^2 \nabla \cdot \underline{u} + C_\gamma p = 0$$

where $C_\gamma > 0$ is a dashpot damping term discussed below. Note that the fluid density ϱ_f is normalized to unity and the equations are written in dimensionless form. The basic idea of the ACM can be traced back to Chorin [9]. More recently, several authors have reconsidered the ACM. Guermond and Mineev state that “the artificial compressibility method may not have been given all the attention it deserves in the literature” [38]. The spirit adopted here, which is to explicitly solve eqns. (2.1, 2.3), is inspired by the work of Ohwada and Asinari [55]. The ACM solution converges to

the solution of the incompressible Navier–Stokes equations (INC) with

$$(2.4) \quad e_{\text{ACM}} = \|\underline{U}_{\text{ACM}} - \underline{U}_{\text{INC}}\|_2 = \mathcal{O}(C_0^{-2})$$

as $C_0 \rightarrow \infty$. Here, \underline{U} is the state vector, containing \underline{u} and p . We will confirm this result numerically later. Note that [55] proposes a strategy to increase the accuracy to $\mathcal{O}(C_0^{-4})$ using Richardson extrapolation, but we do not follow this approach because the second order is sufficient when combined with the volume penalization method. We also point out that there is a natural upper limit for C_0 , which is the true speed of sound of the fluid (*e.g.* $C_0 = 340 \text{ ms}^{-1}$ in air), and that any fluid is at least slightly compressible.

2.2. Volume penalization. The no-slip boundary conditions at the fluid–solid interface are imposed using the volume penalization method [3, 2], which is based on the physical intuition of approximating a solid obstacle as a porous medium with small permeability. The penalized versions of eqns. (2.1, 2.3) are solved in the larger domain $\Omega = \Omega_f \cup \Omega_s$, where Ω_s is the solid domain, and read

$$(2.5) \quad \partial_t \underline{u} + \underline{u} \cdot \nabla \underline{u} + \nabla p - \nu \nabla^2 \underline{u} + \frac{\chi}{C_\eta} (\underline{u} - \underline{u}_s) + \frac{\chi_{\text{sp}}}{C_{\text{sp}}} (\underline{u} - \underline{u}_\infty) = 0$$

$$(2.6) \quad \partial_t p + C_0^2 \nabla \cdot \underline{u} + C_\gamma p + \frac{\chi_{\text{sp}}}{C_{\text{sp}}} (p - p_\infty) = 0,$$

Here χ is the indicator function, $C_\eta \ll 1$ is the penalization parameter (permeability) and \underline{u}_s the solid body velocity field. The indicator function is $\chi = 1$ inside Ω_s and $\chi = 0$ in Ω_f , and we use a thin smoothing layer with thickness proportional to the grid spacing in the case of moving [47] or deforming obstacles [30]. For details on the generation of χ , see [32]. From the penalization term aerodynamic forces are obtained by volume integration [2],

$$\underline{F} = C_\eta^{-1} \int_\Omega \chi (\underline{u} - \underline{u}_s) dV,$$

for which we use the midpoint quadrature rule. We anticipate that the penalization error converges as

$$(2.7) \quad e_{\text{VPM}} = \left\| \underline{U}_{\text{ACM}, C_\eta} - \underline{U}_{\text{ACM}} \right\|_2 = \mathcal{O}(C_\eta^{1/2})$$

for $C_\eta \rightarrow 0$ using similar arguments as for INC.

For our application to unbounded exterior flows, an additional sponge penalization term (index sp) has been added [30, 31], which imposes mean flow conditions, \underline{u}_∞ and p_∞ , in a layer at the outer boundary of the computational domain. Contrarily to the penalization for the obstacle itself, this term also acts on the pressure p . We can understand the ACM as a transport of divergence, which is created both at the boundary and in the nonlinear term. Hence, some outflow conditions are required to remove it from the physical domain, and the sponge term here plays the dual role of absorbing outgoing pressure waves as well as damping outgoing vortical structures.

In the case of impulsively started flow, the initial condition is incompatible with the boundary conditions, which causes a singularity in the aerodynamic force. A strong pressure wave of width $\delta_s = \mathcal{O}(C_\eta C_0)$ is created at the boundary, because the penalization requires a time $\mathcal{O}(C_\eta)$ to damp the velocity inside the obstacle, and the ACM transports it with a speed C_0 . Its intensity decays with the distance R

as $R^{-(D-1)}$, where $D = 2$ or 3 is the dimensionality of the problem. Even though, physically speaking, the pressure wave is an artifact of the ACM, it still needs to be resolved. If δ_s is too small, dispersion errors occur, and spurious oscillations in the forces can appear. In practice, we ensure that $\Delta x \leq \delta_s$. In order to minimize reflections, the width of the sponge layer L_{sp} is set larger than characteristic length scales of the geometry; a wider sponge reduces reflections. We then adjust the sponge constant C_{sp} such that the time the pressure wave spends in the sponge is equivalent to τ times the relaxation time, yielding $C_{sp} = L_{sp}(C_0\tau)^{-1}$. Here we set $\tau = 20$, but found that the specific choice of both τ and L_{sp} only has a weak impact on the solution (see Appendix D for details).

In simulations with periodic boundary conditions, the sponge technique cannot be used. For such cases, we use the dashpot damping term $C_\gamma p$ proposed in [55] to mitigate pressure waves; the constant is then $C_\gamma = 1$, as suggested in [55].

The combination of artificial compressibility and volume penalization constitutes our physical model. It has four parameters (C_η , C_0 , C_{sp} , C_γ), the choice of which will be discussed in detail below.

3. Numerical method and discretization errors. The model equations (2.5-2.6), are discretized in space and time. Spatial derivatives are approximated using centered higher-order finite differences on a collocated, periodic grid. We use the optimized fourth order scheme proposed by Tam and Webb [69] for first order derivatives (Appendix A) and a classical, centered, fourth order stencil for second order derivatives.

Time integration is done with a classical Runge–Kutta-4 scheme. The explicit scheme implies stability restrictions on the time step Δt , namely

$$\Delta t < \min \left(\text{CFL} \Delta x_{\min} / u_{\text{eig}}, \text{CFL}_\eta C_\eta, \text{CFL}_\nu \Delta x_{\min}^2 / \nu \right),$$

where the characteristic velocity is $u_{\text{eig}} = |u_{\max}| + \sqrt{u_{\max}^2 + C_0^2}$, which we can approximate by $u_{\text{eig}} \approx C_0$ as $C_0 \gg |u_{\max}|$. The constants are set to $\text{CFL} = \text{CFL}_\eta = 1.0$ and $\text{CFL}_\nu = 1/4$. We therefore expect the fully discretized solution to converge with 4th order accuracy in space and time,

$$(3.1) \quad e_{\text{FDM}} = \left\| \underline{U}_{\text{ACM}}^{\Delta x, \Delta t} - \underline{U}_{\text{ACM}} \right\|_2 = \mathcal{O}(\Delta x^4) + \mathcal{O}(\Delta t^4),$$

which we will verify later numerically. This is valid in the case without penalization. As pointed out in [54], the discretization (eq. 3.1) and penalization (eq. 2.7) error cannot be treated independently. A too small value for C_η results in a loss of regularity of the exact solution and by consequence the discretization error increases, thus there is an optimal choice of C_η as a function of Δx . As discussed in our previous work [31, 32], the relation is

$$(3.2) \quad C_\eta = (K_\eta^2 / \nu) \Delta x^2$$

where K_η is a constant which depends only on the discretization scheme. It can be interpreted as the number of grid points in the penetration boundary layer inside the obstacle. Using eqn. (3.2), first order convergence [54] is assured for any value of K_η , *i.e.*,

$$(3.3) \quad \left\| \underline{U}_{\text{ACM}, C_\eta}^{\Delta x, \Delta t} - \underline{U}_{\text{ACM}} \right\|_2 = \mathcal{O}(\Delta x) + \mathcal{O}(\Delta t^4),$$

as $\Delta x, C_\eta \rightarrow 0$. The error offset can be tuned by choosing K_η . In the present work, we obtained best results using the same values of $0.05 \leq K_\eta \leq 0.4$ as reported in [32] with a Fourier discretization, which suggests a certain universality of this scaling.

4. Multiresolution analysis, biorthogonal wavelets and thresholding errors. Motivated by the multitude of excited scales in the flow, in particular in the turbulent regime, and close to the boundary, which may even change in time, we introduce dynamically adaptive grids. The grid is supposed to track automatically the motion in both scale and position and allows furthermore its prediction for the next time step. To this end we use multiresolution analysis and decompose the solution into biorthogonal wavelets. First we recall the point-value multiresolution analysis and we give the link with biorthogonal wavelets. Some drawbacks of point-value multiresolution analysis are pointed out and we show how they can be overcome using lifted wavelets. Some details on the parallel implementation are given later in section 6.

For ease of presentation we limit the description to the one-dimensional scalar-valued case, denoted by u . The extension to higher dimension and vector-valued data is outlined at the end of the section.

4.1. Point-value multiresolution analysis. Discrete multiresolution analysis introduced by Harten [39, 40, 41] is well-suited for introducing adaptivity into discretization schemes of PDEs. In particular for finite difference methods the point-value multiresolution [39], which is directly related to the interpolating subdivision scheme by Deslauriers & Dubuc [19, 20], has been designed.

Starting point is a nested sequence of uniform grids at level J , $X^J = \{x_i^J\}_{i=0}^{2^J}$ with an odd number of grid points defined by $x_i^J = i/2^J$ for $i = 0, \dots, 2^J$. The grids satisfy $x_{2i}^{J+1} = x_i^J$ for $i = 0, \dots, 2^J$ and $x_{2i-1}^{J+1} = (x_i^J + x_{i-1}^J)/2$ for $i = 1, \dots, 2^J$.

For the solution u given on the grid X^J we can then define a prediction operator $P_{J \rightarrow J+1} : u(X^J) \rightarrow u(X^{J+1})$ which interpolates values of u onto the next finer grid. For this, we use the fourth order interpolating subdivision scheme [19, 20] to interpolate missing values at x_{2i+1}^{J+1} , *i.e.*,

$$(4.1) \quad u_{2i+1}^{J+1} = -\frac{1}{16}u_{i-1}^J + \frac{9}{16}u_i^J + \frac{9}{16}u_{i+1}^J - \frac{1}{16}u_{i+2}^J.$$

Following Harten, we also define a restriction operator $R_{J+1 \rightarrow J} : u(X^{J+1}) \rightarrow u(X^J)$ which is simply the decimation by a factor of two, *i.e.*, $u_i^J = u_{2i}^{J+1}$. Note that $R_{J+1 \rightarrow J} \circ P_{J \rightarrow J+1} = \text{Id}$. Combining restriction and prediction, detail coefficients can be computed by subtracting the values predicted from the coarse grid from the values at the fine grid. At even grid points the details are zero, while at odd grid points we obtain

$$(4.2) \quad \tilde{u}_{2i+1}^J = u_{2i+1}^{J+1} - P_{J \rightarrow J+1} R_{J+1 \rightarrow J} u_{2i+1}^{J+1}$$

Thus the solution on the fine grid u^{J+1} can be represented as a solution at the coarser grid u^J plus detail coefficients \tilde{u}^J . Iterating this procedure from J down to 1 yields the multiresolution transform. The fine grid solution can be reconstructed by inverting the above procedure. Detail coefficients are mostly significant in regions of steep gradients and discontinuities, and are small or even do vanish in regions where the solution is smooth. They “measure the local deviation from a polynomial” and are obtained as the interpolation error. Thus adaptivity can be introduced by removing small detail coefficients without losing the precision of the computation.

4.2. Biorthogonal wavelets. The point-value multiresolution analysis is intimately related to biorthogonal wavelets, as already pointed out by Harten [39], and

the solution $u \in C^0(\mathbb{R})$ can be expanded into a biorthogonal wavelet series,

$$(4.3) \quad u(x) = \sum_{i \in \mathbb{Z}} \langle u, \widetilde{\phi}_i^0(x) \rangle \phi_i^0(x) + \sum_{J=0}^{\infty} \sum_{i \in \mathbb{Z}} \langle u, \widetilde{\psi}_i^J(x) \rangle \psi_i^J(x)$$

Note that for a given primary scaling function ϕ , different dual scaling functions $\widetilde{\phi}$ can be constructed (and vice versa) and thus the choice is not unique and there is some flexibility compared to the orthogonal case (in terms of symmetry, number of vanishing moments, filter length, etc.). For orthogonal wavelets we have $\widetilde{\phi} = \phi$ and $\widetilde{\psi} = \psi$.

For the point-value multiresolution the scaling function ϕ (Fig. 1) is identical to the Deslauriers–Dubuc fundamental function [19, 20]. It can be obtained by interpolating a delta Dirac impulse (using Lagrange interpolation), and the filters are defined to be symmetrical and have minimal support for a given polynomial order. They are equivalent to the autocorrelation function of orthogonal Daubechies [14] scaling functions [51]. The dual scaling functions are delta Dirac distributions $\widetilde{\phi}_k^J(x) = \delta(x - x_k^J)$. The wavelets are interpolating ('interpolets'), yield an interpolating subdivision scheme, and correspond to a shifted scaling function $\psi(x) = \phi(2x - 1)$, while the dual wavelets are linear combinations of δ distributions. The construction of these interpolating wavelets was also proposed by Donoho [25] and rediscussed later by Sweldens [67]. Note that the primary scaling function is normalized with respect to the L^∞ norm, *i.e.*, $\phi_i^J(x) = \phi(2^J x - i)$ implying $\|\phi_i^J\|_\infty = 1$, and not with respect to the L^2 norm, as it is typically the case.

Both scaling functions and wavelets fulfill refinement relations,

$$(4.4) \quad \phi(x) = \sum_{n \in \mathbb{Z}} h_n \phi(2x - n) \quad \widetilde{\phi}(x) = \sum_{n \in \mathbb{Z}} \widetilde{h}_n \widetilde{\phi}(2x - n)$$

$$(4.5) \quad \psi(x) = \sum_{n \in \mathbb{Z}} g_n \phi(2x - n) \quad \widetilde{\psi}(x) = \sum_{n \in \mathbb{Z}} \widetilde{g}_n \widetilde{\phi}(2x - n)$$

and the filter coefficients are coupled via $\widetilde{g}_n = (-1)^{1-n} h_{1-n}$ and $g_n = (-1)^{1-n} \widetilde{h}_{1-n}$.

Rearranging the restriction and prediction operations of the multiresolution transform yields the filter coefficients and applying the fast wavelet transform with these filters and downsampling will yield equivalent results. The detail coefficients correspond to the wavelet coefficients. For the point-value multiresolution we have $\widetilde{h}_0 = 1$ and $\widetilde{h}_n = 0$ for $n \neq 0$ and thus $g_1 = 1$ and $g_n = 0$ for $n \neq 1$. The coefficients of h and \widetilde{g} depend on the interpolation order, and in the linear case we have $h_n = \{1/2, 1, 1/2\}_{n=-1,0,1}$ and $\widetilde{g}_n = \{-1/2, 1, -1/2\}_{n=0,1,2}$.

The filter \widetilde{h} illustrates the loose downsampling of the data (simple decimation by a factor of two) when going to coarser scale and it is thus not a low pass filter in the classical sense as no high frequency contributions are eliminated. The corresponding scaling function $\widetilde{\phi}$ is a distribution, and even not in $L^2(\mathbb{R})$. The wavelet ψ is a shifted scaling function and hence not a wavelet with vanishing mean. The corresponding filter g is thus not a band pass filter neither.

These wavelets resulting from Harten's point-value multiresolution are Cohen–Daubechies–Feauveau (CDF) biorthogonal wavelets [12] which are symmetric and compactly supported. For cubic interpolation we have CDF 4/0 wavelets, because the analyzing wavelet has 4 vanishing moments while the synthesizing one has zero vanishing moments. The corresponding filter coefficients h, g and $\widetilde{h}, \widetilde{g}$ are summarized in the appendix B and the functions are shown in Fig. 1.

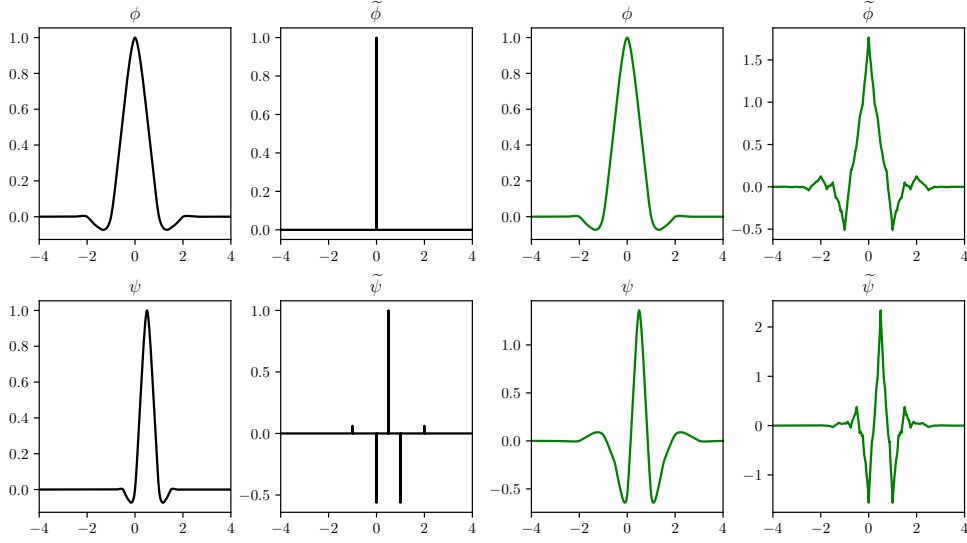


FIGURE 1. Scaling functions ϕ , wavelets ψ and dual functions $\tilde{\phi}$, $\tilde{\psi}$ for the CDF 4/0 (left, black) and CDF 4/4 wavelets (right, green).

This biorthogonal wavelet decomposition yields good compression properties of the data, as the analyzing wavelet $\tilde{\psi}$ has vanishing moments. However there is no separation into scales with separated frequency bands, as the loosely downsampling does not filter out high frequency contributions (it produces aliasing) and the synthesizing wavelet has no vanishing moment which means that all frequencies are mixing up. For denoising [26] and Coherent Vorticity Simulation [33] such decompositions are only of limited use and for this reason we are applying Sweldens' lifting scheme to construct second generation wavelets. The CDF 4/0 biorthogonal wavelets are upgraded to CDF 4/4 [67, 66, 68] which yield a reasonable scale and frequency separation.

4.2.1. Lifted biorthogonal wavelets. To improve the frequency selectivity of the point-value multiresolution decomposition we apply (primary) lifting to the wavelet ψ and thus construct a wavelet with vanishing moments. To this end we modify the primary wavelet ψ and the dual scaling function $\tilde{\phi}$ correspondingly, while the secondary wavelet $\tilde{\psi}$ and the primary scaling function ϕ remain unchanged. For the filters the lifting operations are applied accordingly [66]. More precisely we determine lifting coefficients s_n such that

$$(4.6) \quad \psi(x) = \psi^{\text{old}}(x) - \sum_n s_n \phi^{\text{old}}(2x - n)$$

$$(4.7) \quad \tilde{\phi}(x) = \sum_n \tilde{h}_n \tilde{\phi}^{\text{old}}(2x - n) + \sum_n s_n \psi^{\text{old}}(x - n)$$

requiring that the new ψ has M vanishing moments, *i.e.*, $\int x^p \psi(x) dx = 0$ for $p = 0, \dots, M - 1$. In the linear interpolation case, *i.e.*, CDF 2/0, we have $s_0 = s_1 = -1/4$ and for the resulting lifted filters we get $\{g_n, n = -3, \dots, 1\} = \{1/8, -1/4, 3/4, -1/4, -1/8\}$ and $\{\tilde{h}_n, n = -2, \dots, 2\} = \{1/8, -1/4, -3/4, -1/4, 1/8\}$, yielding thus CDF 2/2 wavelets, which have two vanishing moments. Applying lifting to the cubic inter-

polatory wavelets CDF 4/0 we can construct CDF 4/4. They are shown in Fig. 1 and the filter coefficients are given in the appendix B.

4.3. Nonlinear approximation and thresholding. The biorthogonal wavelet representation of the solution u (eqn. 4.3) can be used for introducing an adaptive grid. To this end we apply thresholding to the detail coefficients $\tilde{u}_i^J = \langle u, \tilde{\psi}_i^J(x) \rangle$ and mark details with magnitude below a constant, level-independent threshold C_ε , precisely if $|\tilde{u}_i^J| / \|u\|_\infty < C_\varepsilon$. As a detail coefficient \tilde{u}_i^J is directly related to a grid point x_{2i+1}^{J+1} , we could remove the corresponding grid points. In our block-based structure, a block is coarsened only if *all* its details are smaller than C_ε , *i.e.*, some insignificant points can be included. The thresholding error can be estimated in the L^∞ norm and is directly proportional to the threshold, *i.e.*, after N_t time steps we have,

$$(4.8) \quad \left\| u_{\text{ACM}}^{\Delta x, C_\varepsilon} - u_{\text{ACM}}^{\Delta x} \right\|_\infty \stackrel{\text{def}}{=} e_{\text{MR}} \leq N_t C_\varepsilon$$

as shown in [13, 60]. This upper bound assumes a worst-case scenario that the filtering introduces an error $\mathcal{O}(C_\varepsilon)$ in all N_t time steps, which of course depends on the problem. For example in pure transport, the production of fine scales is related only to the lack of translation invariance of the multiresolution transform. Eventually, if no velocity is imposed, the error is in fact $e_{\text{MR}} \leq C_\varepsilon$. Thus, whether the number of time steps enters eqn. (4.8) depends on the non-linearity. Assuming the pure transport CFL condition, we have $N_t \propto \Delta x^{-1}$.

4.4. Extension to higher dimensions and vectors. Extensions in dimension larger than one are obtained by tensor product of the one-dimensional wavelets. For multiresolution constructions in two dimensions we obtain wavelets in the horizontal, vertical and diagonal directions, while in three dimensions we have seven directions. For details we refer to [51]. For vector-valued quantities, *e.g.*, the state vector \underline{U} , the biorthogonal wavelet expansion is applied to each component of the vector and thus a vector-valued wavelet series is obtained. Hence the coefficients become vector-valued, but not the basis functions. During thresholding, each component is normalized by its L_∞ -norm.

4.5. Grid prediction and time stepping algorithm. The algorithm to advance the numerical solution $\underline{U}(t^n, \underline{x})$ (state vector containing \underline{u} and p) on the block-structured grid \mathcal{G}^n to the new time level t^{n+1} is as follows:

1. Refinement. Given $\underline{U}(t^n, \underline{x})$ on the grid \mathcal{G}^n , we first extend the grid by adding neighbors in position and scale. This concept of a safety zone, introduced in [49], ensures that the solution is tracked in scale and space. Adding neighbors in scale captures newly emerging scales due to the quadratic non-linearity, which can produce scales twice as small in one time step. The grid \mathcal{G}^n is thus extended to $\tilde{\mathcal{G}}^n$ by refining all blocks by one level.
2. Evolution. On the extended grid $\tilde{\mathcal{G}}^n$, we solve equations (2.5–2.6) using finite differences with explicit time-marching.
3. Coarsening. We compute the detail coefficients of $\underline{U}(t^{n+1}, \underline{x})$ for each block, and tag it for coarsening if the largest detail is smaller than the prescribed threshold C_ε . Next, the tag is removed if coarsening would result in a non-graded grid, and finally the tagged blocks are merged with their sister blocks. This procedure is repeated until no more blocks can be coarsened.

This well established algorithm (see, *e.g.*, [49, 62, 24, 45, 46]) is at the core of our adaptive strategy. In practice, the above algorithm is modified by imposing an upper

bound for the refinement, *i.e.*, a level J_{\max} is introduced at which no refinement is allowed anymore. The largest possible value in the current implementation is $J_{\max} = 18$. This is done not only because of finite computational resources, but also in the interest of balancing the discretization- and thresholding error. While the former error depends mainly on Δx (and thus directly on J_{\max}), the latter is determined by C_ε . The relation between both is discussed below.

If the maximum level J_{\max} is reached after the refinement stage and the detail coefficients are significant after the evolution step, we can choose between two possibilities: either, the corresponding block is coarsened, even though its details are significant, or it remains at J_{\max} . The former option corresponds to dealiasing and avoids accumulation of energy in high wavenumbers, if viscous dissipation is not sufficient to stabilize the simulation. We therefore term this option “dealiasing”. In low Reynolds number simulations, it can be omitted for the benefit of improved precision, while in most simulations it is required for stabilization.

While the volume penalization term does usually result in large detail coefficients near the fluid-solid interface, it can happen that for large values of C_ε the grid is coarsened at the interface. In this case, oscillations appear in the aerodynamic forces, which are undesirable. Therefore, we use the mask function χ as secondary criterion for block coarsening, and apply the same multiresolution thresholding with $C'_\varepsilon = 10^{-6}$ to it. Thus, blocks containing the fluid-solid interface are coarsened only if the dealiasing option is used. The initial condition at $t = 0$ is created in an iterative process and also takes the mask χ into account.

5. Balancing modeling, discretization and thresholding errors. The numerical solution of the Navier–Stokes equations with artificial compressibility on adaptive grids and volume penalization involves in total five parameters, ACM (C_0), penalization (C_η), time (Δt), space (Δx) and thresholding (C_ε). The accuracy of the computation with respect to the reference solution, *i.e.*, the exact solution of the incompressible Navier–Stokes equation, can be estimated from the various error contributions, namely, the artificial compressibility (eq. 2.4), penalization (eqn. 2.7), discretization (eqn. 3.1) and thresholding (eqn. 4.8) errors and then applying the triangle inequality, we find,

$$(5.1) \quad \left\| U_{\text{ACM}, C_\eta}^{\Delta x, \Delta t, C_\varepsilon} - U_{\text{INC}} \right\|_2 \leq \mathcal{O}(C_0^{-2}) + \mathcal{O}(C_\eta^{1/2}) + \mathcal{O}(\Delta x^4) + \mathcal{O}(\Delta t^4) + \mathcal{O}(C_\varepsilon)$$

A suitable choice of the parameters taking their scaling into account allows to balance the different errors. In sec. 3 we also already discussed the balancing of discretization and penalization errors, which formally reduces the convergence in Δx to first order, (eqn. 3.3). Requiring all errors to decrease simultaneously by the same amount, we find in the case without penalization the following relations

$$(5.2) \quad C_\varepsilon \propto \Delta x^5 \qquad C_0 \propto \Delta x^{-2},$$

while in the penalized case we have

$$(5.3) \quad C_\varepsilon \propto \Delta x^2 \qquad C_0 \propto \Delta x^{-1/2} \qquad C_\eta = (K_\eta^2/\nu) \Delta x^2,$$

where $0.05 \leq K_\eta \leq 0.4$. In addition, as described above, we fix the sponge constant to $C_{\text{sp}} = L_{\text{sp}}/C_0\tau$ with $\tau = 20$. Asymptotically, the restriction on Δt due to the penalization term is stronger than the classical CFL condition. For this reason we can increase the scaling to $C_0 \propto \Delta x^{-1}$ for high resolutions without decreasing the

time step further and thus at no extra cost. Note that using this modified scaling, the condition $\delta_s = C_0 C_\eta = \mathcal{O}(\Delta x)$ is ensured for all Δx smaller than a reference value, provided the condition is met with that reference.

6. Parallel implementation.

6.1. Data structure. Previous work on wavelet-based adaptivity exploited the fact that the fast interpolating wavelet transform can be used to assign one wavelet coefficient to each grid point, and hence allows judging for each point if it is important or can be discarded [43]. The resulting grids are as sparse as possible, and each point is a node in a tree data structure [60] or hash-table [53]. The difficulty is that these data structures are poorly aligned with the memory access of typical modern CPUs. If the CPU requires a data point for computing, the vicinity of this point in the 1D memory is also transferred to the CPUs cache, which explains the high performance of structured grids. To turn the achievable sparsity into CPU time compression, a block-based hybrid data structure is a suitable choice. In the context of wavelet-based multiresolution, block-based grids have first been proposed by Domingues et al. [24] and later, independently, in [58]. The basic idea is however older; for adaptive computations without wavelet-support, they have been pioneered by Berger and Collela [5] and further developed by Deiterding and coworkers [15, 16, 17]. An excellent overview over recently developed software packages can be found in [63].

Block-based grids are locally structured and for the relations between blocks, a flexible data structure has to be used. In our implementation, we use a tree-based structure for this task, and define blocks of size B_s^D . All blocks have the same number of points, which is the same in all directions. The number of entries in the tree data structure, and thus its overhead, is reduced by the same factor B_s^D . On the other hand, the total number of grid points N_{points} is increased, until for (very) large B_s , an equidistant monoblock grid is recovered. Figure 2 illustrates the concept of our data structure. The grid layout contains blocks of the same size on different levels, while the memory layout is a simple, contiguous array of size $B_s \times B_s \times B_s \times N_b$. Since the number of blocks N_b changes during the simulation, our code allocates an array with the largest possible number of blocks for the given memory, which is specified in the program call using the flag `--memory=40.0GB`. Memory allocation is done once during the initialization and is not deallocated again until the termination of the code. This type of memory management is suitable for high-performance supercomputers, where typically only one application is running on a given processor.

Since the number of blocks N_b in the tree data structure is typically low ($N_b = \mathcal{O}(10^5)$ blocks, while $N_{\text{points}} = N_b(B_s - 1)^D = \mathcal{O}(10^{10})$ in 3D applications), we design a simple tree library based on the work of Gargantini [34, 35], where octal numbers are used to encode the position of an element in the tree. There is thus no need to use an external high-performance tree library, such as `p4est` [8]. From the octal number, level and position of the block can be computed, as well as the IDs of neighboring blocks. It constitutes, along with a refinement flag and level indicator, the metadata, which is separated from the actual block data named heavy data. The metadata is stored redundantly on all CPUs and is kept synchronized, so that neighbor lookup is a local process, while the heavy data is process-local.

6.2. Parallelization aspects. Parallelization appears in our implementation at two places: ensuring that each MPI rank has the same amount of blocks to compute (load balancing) and then synchronizing the layer of ghost nodes.

The creation and removal of blocks during the simulation can lead to an imbal-

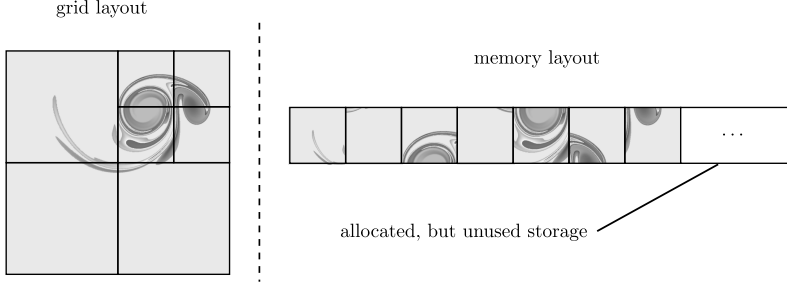


FIGURE 2. *Data structure. Left: grid layout, composed of 7 blocks of the same size but at different positions and levels. Right: memory layout, the grid is stored as simple, contiguous array. Memory allocation done once on startup, but only the portion required at time t is used.*

anced distribution of blocks among processes. As we use blocks of identical size, load balancing is guaranteed if the number of blocks on each process is the same. The load balancing process first computes the index of all blocks on a space-filling Hilbert-curve [70, 42], then distributes contiguous chunks of blocks to the processes. Special care is devoted to keeping the required number of transfers as small as possible. The Hilbert-curve preserves the locality of blocks and minimizes the interface between processes.

Any parallelization by decomposition of the domain requires communication between the processes, either in the form of flux transfer or ghost node synchronization. Our blocks are equipped with a layer of n_g ghost nodes (where n_g depends on the support of the interpolation and discretization stencils) that overlaps with adjacent blocks. During the synchronization of the ghost nodes, the processes first prepare the required data, *i.e.*, apply restriction and prediction operators if required, and copy them into a buffer, which is then sent to the receiving process. The receiver then extracts the data to the ghost node layers of each block. We skip more details on this technical part in the interest of brevity.

Parallelization of an adaptive code is inherently more complicated than in the case of static grids. The number of blocks can vary significantly during a simulation and choosing the same number of processes throughout the simulation is often not an efficient choice. On most supercomputers, a simulation is interrupted after a wall time limit is exceeded, which is usually of the order of 24h. We exploit this fact to decide upon resubmission of a simulation if the number of CPUs is increased, decreased or can remain unchanged. We will discuss the performance in greater detail in section 8.

7. Numerical results.

7.1. Three vortices. As a quantitative validation test for the fluid part in two-dimensions, we consider the vortex merger proposed in [44]. The setup involves no walls and is a good starting point for the validation of our new numerical method. At time $t = 0$, three Gaussian vortices (Fig. 3A) are set into the periodic domain of size $L = 2\pi$, two with positive ($\Gamma = 1$) and one with negative ($\Gamma = -1/2$) circulation. The initial vorticity field is given by

$$\omega(x, t = 0) = \sum_{i=1}^3 \frac{\Gamma_i}{\pi \cdot a^2} \exp\left(-((x - x_{0,i})^2 + (y - y_{0,i})^2)/a^2\right),$$

where $a = 1/\pi$ and the vortex centers $(x_{0,i}, y_{0,i})$ are located at $(0.75, 1)\pi$, $(1.25, 1)\pi$ and $(1.25, 1.25)\pi$. Note that initially, the mean vorticity is small but not zero. The

vortices then interact nonlinearly, but the evolution remains deterministic. Due to the low viscosity of $\nu = 5 \cdot 10^{-5}$, thin vortex filaments develop during the merging of the two positive vortices (Fig. 3B). We stop the simulation at $t = 40$ (Fig. 3C), and use this time instant for comparing different simulations. The creation of small scales due to the nonlinearity is an important test for our adaptive framework.

We perform four types of numerical simulations for this problem:

1. Incompressible Navier–Stokes (INC) solved with a Fourier pseudospectral method [32], which is the quasi-exact reference solution,
2. ACM solved with a Fourier pseudospectral method, as quasi-exact solution of the ACM equations,
3. ACM solved with the fourth-order finite difference method on equidistant grids,
4. ACM solved with the fourth-order finite difference method on dynamically adaptive grids using multiresolution analysis with CDF 4/0 and CDF 4/4 wavelets.

Those simulations allow us to assess (i) the model error of the ACM, (ii) the discretization error and (iii) the thresholding error. Combined, they allow us to confirm the relation between the three parameters of the problem (C_0 , Δx , C_ε) presented in eq. (5.2). Instead of Δx , it is however more practical to use the maximum refinement J_{\max} , which is related to Δx via $\Delta x = 2^{-J_{\max}} L / (B_s - 1)$. In all ACM simulations problem, we set the pressure damping $C_\gamma = 1$, as the sponge technique cannot be used for periodic domains.

(i) *Compressibility error.* We first consider the spectral solution of the artificial compressibility eqns. (2.5–2.6). Comparing the spectral ACM simulations with the incompressible reference solution from [44] allows us to evaluate the compressibility error alone. We compute the reference solution with spatial resolution of 1536×1536 modes using the FLUSI code [32], which uses the same Fourier pseudospectral scheme as in [44]. Time integration is done with the classical 4th order Runge–Kutta scheme and CFL = 1.5. For all times $t \geq 0$, we verified that the isotropic Fourier spectrum decays exponentially for large wavenumber k below machine precision, hence both the reference solution and the spectral ACM simulations can be considered highly accurate. Figure 3D shows the resulting convergence in C_0 , confirming the second order convergence from eq. (2.4).

(ii) *Discretization error.* We next evaluate the discretization error of the finite difference scheme on equidistant grids, fixing $C_0 = 10$ for computational convenience, and compare with the spectral solution of the ACM equations. The equidistant computations with resolutions from $N = 256$ to 4096 are performed using the WABBIT code with adaptivity turned off. In this test case, the viscosity is sufficiently elevated to stabilize the simulation without filtering at the maximum level J_{\max} . Therefore we perform three types of equidistant computations shown in Fig. 3E, CDF 4/0 (red line), CDF 4/4 (green) and without (orange) the dealiasing filter. Without dealiasing, the method is clearly fourth order accurate. If filtering at J_{\max} is used, the CDF 4/4 solution increases, as expected, slightly the error compared to the case without any filtering. Note that filtering is usually required for stabilization. The convergence rate locally varies, but a linear least squares fit to the data reveals a slope of 4.04. With the CDF 4/4 wavelet, we can hence preserve the accuracy. The CDF 4/0 method on the other hand significantly increases the error and deteriorates the convergence rate. This could be due to the lack of scale separation in the CDF 4/0 wavelet.

(iii) *Thresholding error.* We now consider fully adaptive simulations, where we fix $C_0 = 10$ and use the refine – evolve – coarsen cycle in each time step to remove aliasing

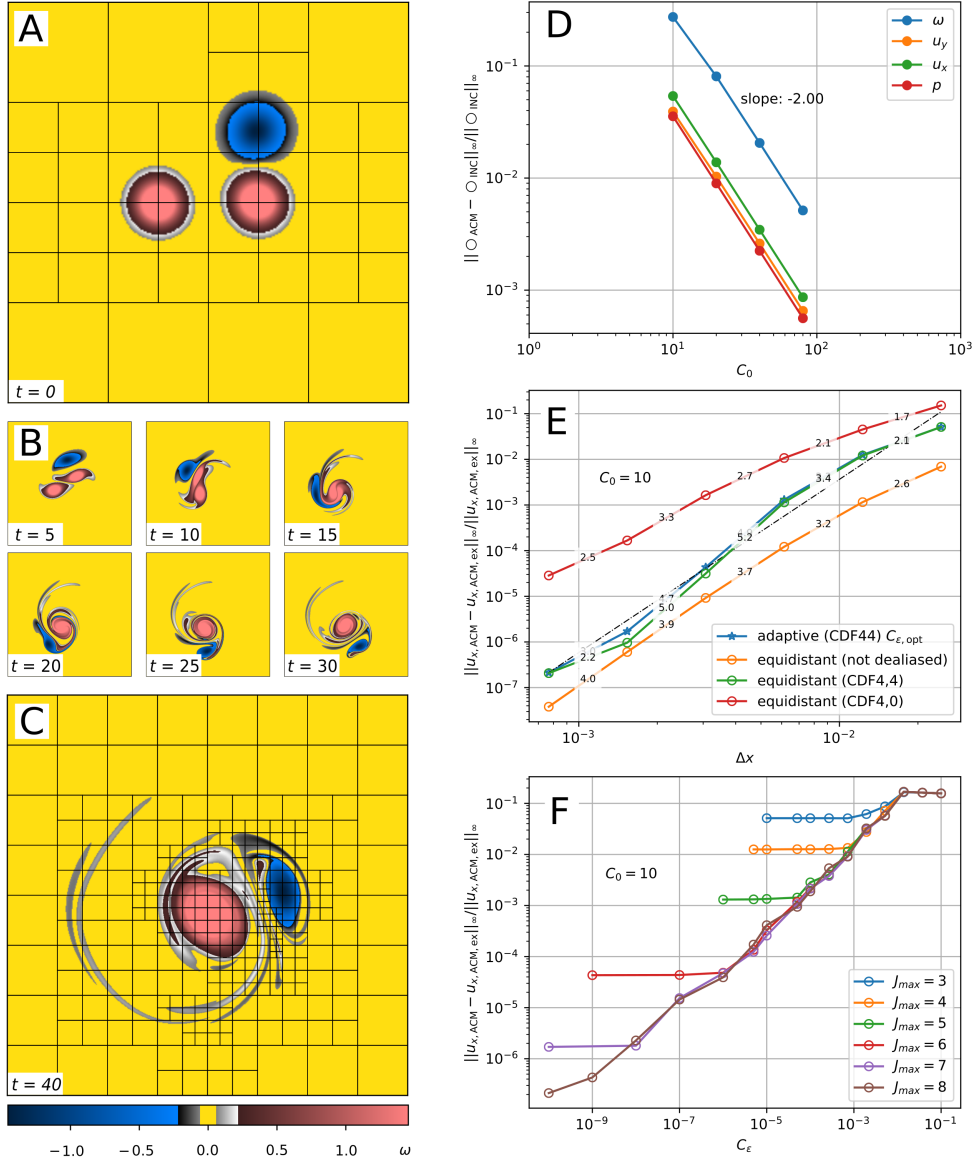


FIGURE 3. *Three vortices simulations. A-C: Time evolution of the vorticity field in a simulation with $B_s = 33$, $C_\epsilon = 10^{-5}$, $J_{\max} = 8$ and $C_0 = 10$. Initial condition (A), intermediate (B) and final time (C). D: Decay of the compressibility error with respect to the incompressible solution as a function of C_0 , computed using a non-adaptive spectral discretization. Second order is observed. E: Decay of the error w.r.t the spectral ACM solution as a function of Δx for $C_0 = 10$. Shown are equidistant computations with and without aliasing and adaptive simulations with C_ϵ small enough for the discretization error to be dominant. The black dashed line is a linear least squares fit to the CDF 4/4 data and has a slope of 4.04. The adaptive solution preserves the accuracy of the equidistant ones. F: Decay of the error using CDF 4/4 w.r.t. the spectral ACM solution as a function of C_ϵ for different J_{\max} and $C_0 = 10$. Leftmost points of each line are also shown in E.*

errors. The block size B_s is mainly a parameter that impacts the computational efficiency, which is crucial only for 3D simulations. We here fix $B_s = 33$ for all 2D simulations and discuss the performance as a function of B_s later in section 8. Two snapshots of an adaptive computation are shown in Fig. 3A,C. Visibly, the initial grid contains less blocks than the terminal one. The refinement is concentrated, as expected, in regions with sharp gradients.

In adaptive simulations, the thresholding error arises in addition to discretization and compressibility errors. We compare with the spectral ACM solution for C_0 fixed, hence the compressibility error is absent. Figure 3F shows the error as a function of C_ε for different J_{\max} . For large C_ε , all simulations run on the coarsest possible level ($J_{\max} = 1$) and therefore yield the same error. When C_ε is decreased, the error generally decreases, until a saturation at a level-dependent value of $C_{\varepsilon,\text{opt}}(J_{\max})$ is observed. At this point, the discretization- and thresholding error are of the same size. Decreasing C_ε further can thus not increase the precision, as the discretization error then dominates. Before the saturation, the error decays $\propto C_\varepsilon$. Fig. 3E shows the convergence as a function of Δx (blue line), where we use the smallest C_ε used for each J_{\max} . The obtained curve overlaps the equidistant one almost perfectly – we can hence conclude that we preserve the accuracy and the order of the discretization scheme on adaptive grids (cf also Appendix C for the case of a linear PDE).

7.2. Impulsively started cylinder. We now consider an impulsively started cylinder at $Re = Du_\infty/\nu = 3000$ and compare with [48, 45, 36]. The volume penalization method is used to approximate the Dirichlet boundary condition, and the simulation is two-dimensional. A significant improvement with respect to spectral simulations is that the adaptive framework allows for setting very large domains (for the cylinder simulations, we use here $L = 160$), because the strongest refinement is located near the cylinder. The flow is impulsively started, *i.e.*, the initial velocity is $\underline{u}(\underline{x}, t = 0) = \underline{u}_\infty$, where $\underline{u}_\infty = (1, 0)^T$, and $p(\underline{x}, 0) = 0$. Four levels of resolution are performed, with their key parameters summarized in Fig. 4A. Because of the large computational domain, the coarsest simulation already uses $J_{\max} = 12$ scales.

When using the volume penalization method, we found only minor differences between a simulation with CDF 4/0 and CDF 4/4 wavelets, despite a significantly reduced grid density by about 20%, but since the larger ghost node layer increases the MPI synchronization cost, the overall efficiency was lower when using CDF 4/4 wavelets. Therefore, all following results with penalization are obtained with CDF 4/0.

Figure 4C shows the vorticity field at the final time $t = 3.0$ for the lowest and highest J_{\max} . The vorticity is visually very similar to results presented in the literature [48, 45, 36], and the two simulations show only little differences. Two main vortices are visible behind the cylinder, and secondary and tertiary vorticity lead to a dipole-like flow pattern near the separation point [48].

The drag force is shown in Fig. 4D together with the reference data and an incompressible spectral simulation with penalization [32] (using $L = 20$, 16384×16384 modes, $K_\eta = 0.1$). During the impulsive startup phase, present results obtained with ACM differ as expected significantly from the reference solutions. While the force is very large in the beginning, it later decreases and even becomes negative. After some time, depending on C_0 , the drag however approaches the reference curves. We also note that there is some spread in the reference drag data, and thus we do not present convergence plots for the error.

As discussed, the impulsive start results in pressure waves propagating in the

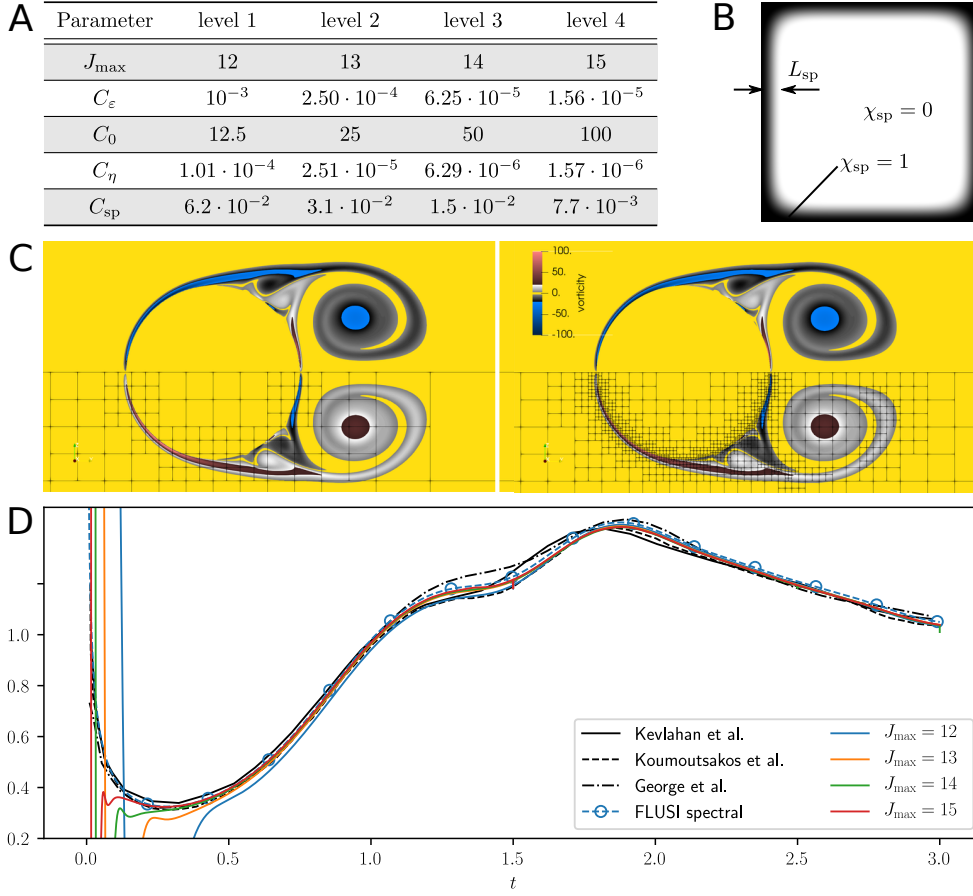


FIGURE 4. *Impulsively started cylinder at $Re = 3000$. A: computational parameters for the four levels of resolution. B: mask function χ_{sp} for the sponge. The actual cylinder is not visible due to the large domain size. C: vorticity field with the block-based grid superimposed in the lower half, results from the level 1 and 4 computations, respectively. G: drag force as a function of time, compared with results from the literature. All results are obtained with CDF 4/0 wavelets.*

domain, and they can contribute significantly to the number of blocks used in the simulation. The pattern is similar in all simulations: the initial wave entails an increasing N_b , until the wave is absorbed by the sponge (Fig. 4B). Then, the grid density rapidly decreases and then remains practically constant. In all cases, less than 0.1% of the corresponding full grid is used at most, which is also related to the large domain size.

7.3. A flapping wing. As example of a time-dependent geometry in 3D, we consider the test case proposed by Suzuki et al. [65], Appendix B2. It has also been considered as validation case in our previous work [32] and by Dilek et al. [22]. We therefore limit the description of the setup to a minimum and refer the reader to [32] for details of the geometry and wingbeat kinematics. The test consists of a single, rectangular flapping wing with finite thickness h and length $R = 1$. No inflow is imposed; the setup mimics hovering flight. The wing moves in an horizontal stroke plane, its prescribed wingbeat motion is visualized in Fig. 5A. The two half cycles, conventionally termed up- and downstroke, are symmetrical. The size of the

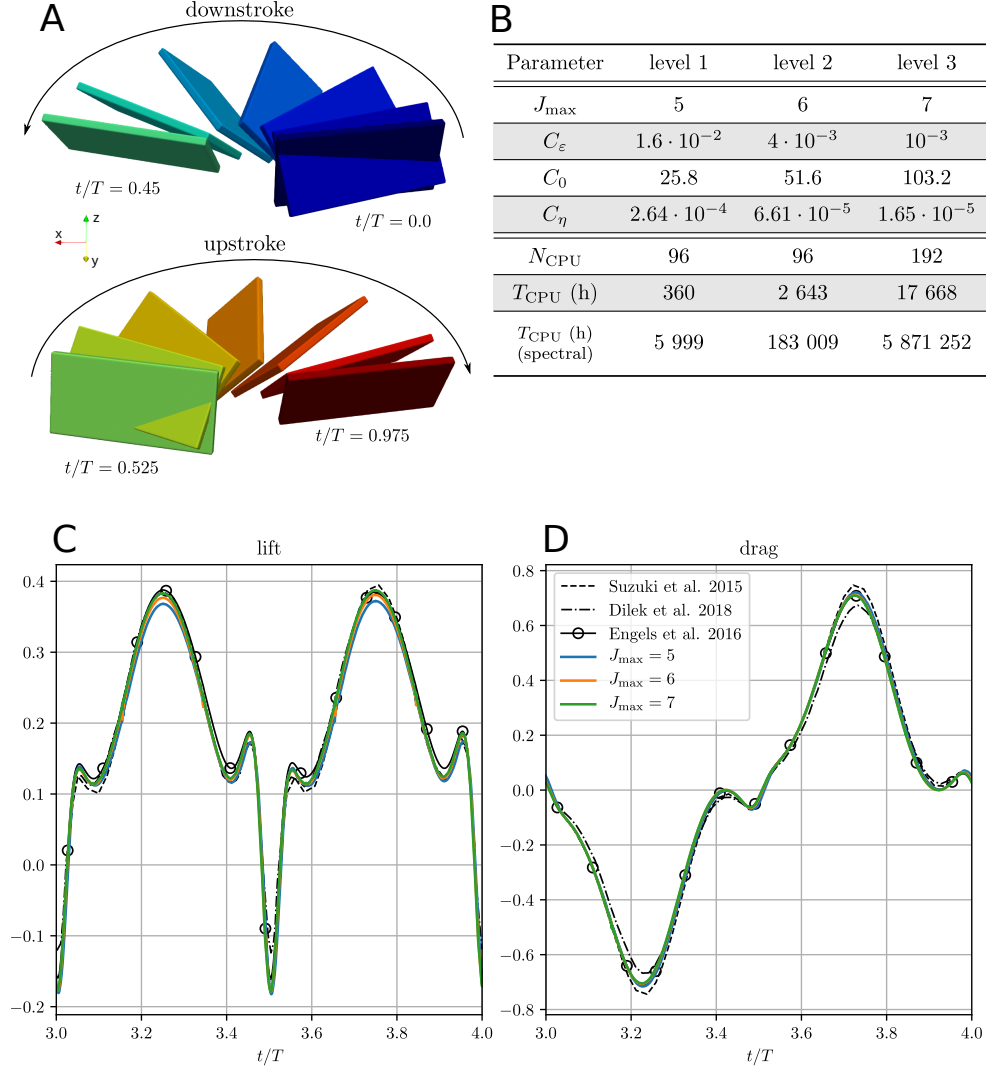


FIGURE 5. Suzuki test case. *A*: visualization of the wing beat. The wing moves in an horizontal stroke plane with varying angle of attack, the motion is symmetrical in down- and upstroke. *B*: computational parameters used in the simulations, together with overall computational cost for the adaptive and spectral codes. *C-D*: Time evolution of lift and drag and comparison with results from the literature. All results are obtained with CDF 4/0 wavelets.

computational domain is chosen large enough to be a good approximation for an unbounded flow, in our case we set $6R \times 6R \times 6R$, which is slightly larger than [65, 22]. At the outer border, we impose homogeneous Dirichlet conditions on $\underline{u}_\infty = 0$ and $p_\infty = 0$ using the sponge term in eqns. (2.5-2.6). The sponge mask is the same as shown in Fig. 4B. The initial condition is fluid at rest, which is incompatible with the boundary condition of the moving wing, like it was above in the cylinder simulations.

As penalization is used for the wing, the scaling relations (5.3) are used, and we use the constant $K_\eta = 0.365$ justified from our previous work [32]. Figure 5B summarizes the parameters used for a coarse, medium and fine resolution simulation.

The low Reynolds number of $Re = u_{\text{tip}} c_m / \nu = 100$, which is comparable to that of a fruit fly, results in a smooth flow topology. Here, u_{tip} is the mean wingtip velocity and c_m the chord length. The flow displays the characteristic features of flapping flight, namely a strong leading edge vortex and a wingtip vortex. The computational grid shows the expected refinement near the wing, while the resolution in the remaining parts of the domain is dictated by gradedness. Because of the absence of fine-scale structures in the flow, the grid is in practice determined uniquely by the mask function χ , and the parameter C_ε is not important. Nonetheless, C_ε has been scaled according to eq. (5.3) for consistency. We set a block size of $B_s = 23$ (see section 8).

Figure 5C-D compares the lift- and drag force obtained by present simulations with the results obtained by Suzuki et al. [65], Dilek et al [22] and our own work [32]. As already noted by Suzuki in their initial publication using two different solvers, some discrepancy between the reference solutions is observed. The difference, integrated over the stroke period, is of the order of 5%, which is why we do not present convergence plots.

Because the grid density ρ_g does not vary much over time, the same number of CPUs was used during the entire simulation. Figure 5B summarizes the number of CPUs and computational cost. The simulations have been performed on IRENE, a Bull Sequana X1000 supercomputer with 79 488 Intel Xeon Platinum 8168 24C cores¹. For comparison, the computed cost (on the same machine) of the analog simulation using the spectral code FLUSI is also given, where we assume the grid to be uniformly on the finest level and the same number of time steps. This latter assumption is justified by the fact that the restriction $\Delta t < C_\eta$ is the most severe one. We observe a significant improvement of CPU time by a factor of 16, 69 and 208 in the different resolution levels. It is however noteworthy that the relatively high viscosity is challenging for the penalization method, as it requires small C_η and thus small Δt . The testcase is furthermore a worst-case scenario for the spectral code, because the fine resolution is required only on the wings surface as no fine-scale flow structures exist in the wake. The equidistant grid of a Fourier-type code is thus not very efficient.

7.4. Bumblebee in forward flight. The last example in our hierarchy of validation cases is the simulation of a model bumblebee. This model has also been used in our previous work [28, 29] and it was the first model to be studied in fully developed turbulence. The penalization method allows for the inclusion of obstacles of arbitrary complexity, and we hence include the bumblebees body. The wingbeat is illustrated in Fig. 6A. We are considering forward flight, which is why the stroke plane is inclined with respect to horizontal. The wing kinematics differs significantly between down- and upstroke. During the downstroke, also called power-stroke, most of the aerodynamic forces are generated, as the wing moves against the flow direction at elevated angle of attack. The upstroke at much smaller angle of attack primarily serves to enable the next downstroke. Our bumblebee has a Reynolds number of $Re = u_{\text{tip}} c_m / \nu = 2000$ and as such produces a more complicated flow topology than the previous test [29, 27, 28]. The domain size is $L = 8$, the block size is $B_s = 23$ (see section 8) and the other key parameters of three simulations levels are given in Fig. 6B. As the viscosity is weaker than in the Suzuki case, C_η is larger and hence is the admissible Δt , which is why we use the $C_0 \propto \Delta x^{-1/2}$ scaling.

The drag (Fig. 6C) and lift (Fig. 6D) show good convergence and display the

¹<http://www-hpc.cea.fr/en/complexe/tgcc-Irene.htm>

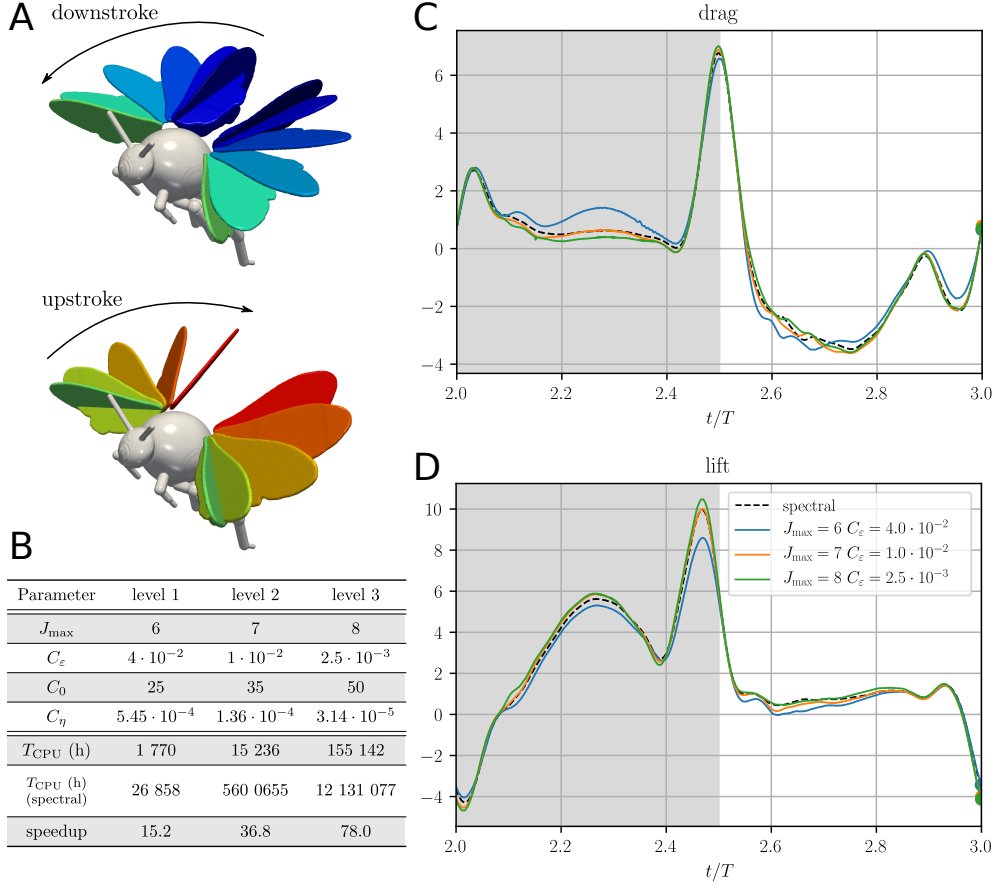


FIGURE 6. Bumblebee simulations. A: Wingbeat of the bumblebee model in forward flight. During the downstroke, the angle of attack is more elevated than during the upstroke. The stroke plane is inclined to generate a forward force. B: computational parameters and CPU time consumption for the three levels of simulation. C-D: Drag- and lift force. All results are obtained with CDF 4/0 wavelets.

typical features. The leading edge vortex is built up during the downstroke and reaches its maximum intensity during the mid-downstroke ($t = 2.25$), which is seen in the lift force as a maximum. At the turning point ($t = 2.5$) between down- and upstroke, the rapid wing rotation causes large peaks in the forces.

The total CPU time (Fig. 6B) increases between levels by a factor of roughly eight, while the factor between two levels of spectral computations is roughly 20. We also note that the speedup of the adaptive code, though also significant at the coarsest level, is improving with increasing resolution. As N_b changes more during a simulation, the number of processes has been adjusted every 24h in the finest simulation (the other two did not require restarting), starting from 624 and ending with 912 processes. Figure 7A,C,E shows the same snapshot of the flow field at $t/T = 2.3$ in all three simulations. Shown is the $|\omega| = 50$ isosurface. Visually, the three levels yield similar results, especially regarding the large scale structures of the flow field. The grid (Fig. 7B,D,F) concentrates, as expected, high resolution near the insect, but parts of the wake now likewise are refined to J_{\max} , because they are detected by the wavelet

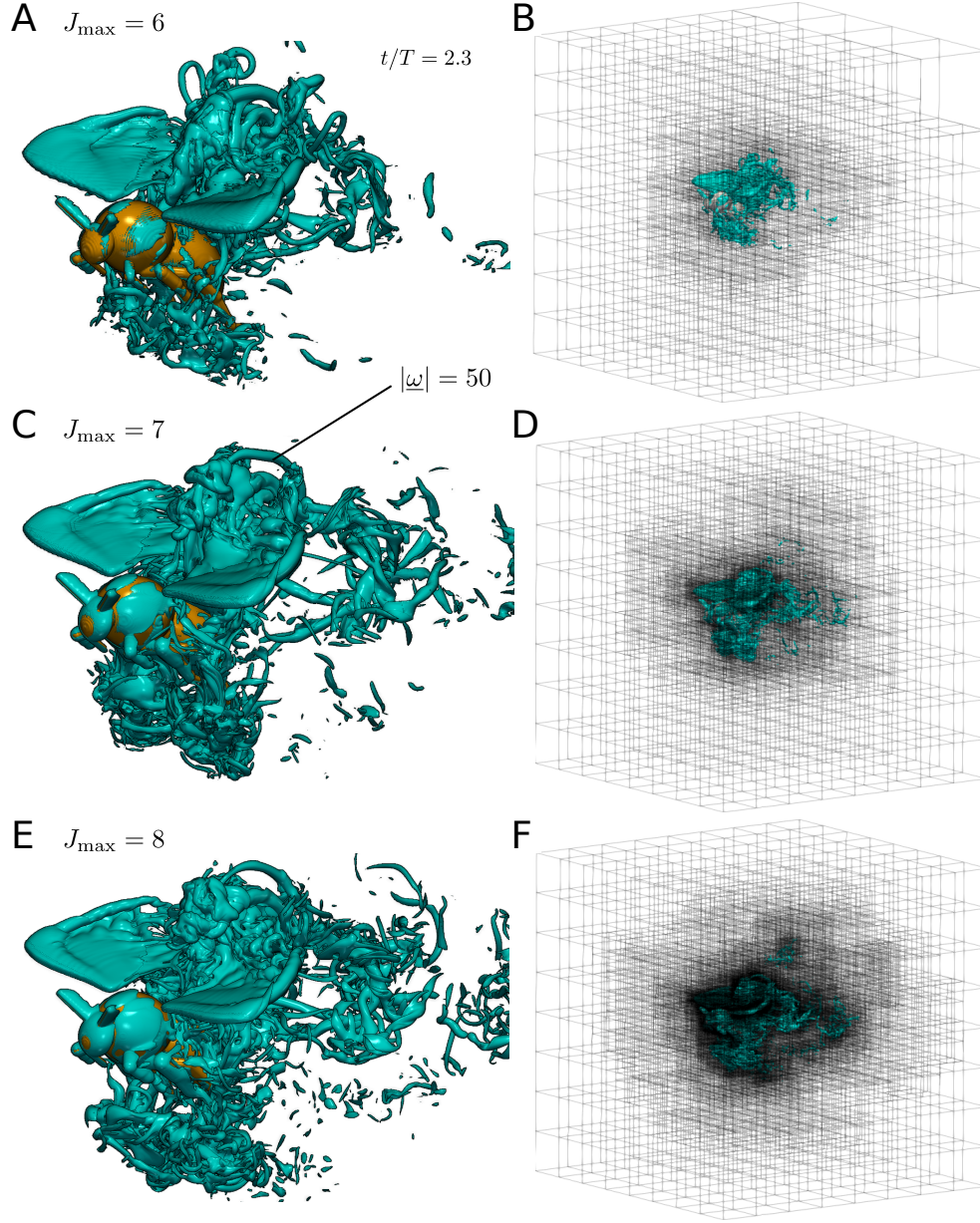


FIGURE 7. *Bumblebee simulations. Visualization of the flow field (isosurfaces of vorticity) at $t/T = 2.3$ (left) and computational grid used at this time (right) for the three simulations. All results are obtained with CDF 4/0 wavelets.*

thresholding.

8. Performance. We have not yet discussed how the block size $B_s = 23$ has been chosen. Prior to performing the actual simulations, we performed a series of runs with varying B_s on the bumblebee configuration. As the smallest Δx depends on B_s , we cannot simply change B_s without altering the results. Therefore, we took advantage of the fact that for an exterior flow, the domain size L is an artifact from the simulation rather than a physical quantity ($L \rightarrow \infty$ in reality). Thus, for every B_s we modified L to obtain the same Δx . All simulations are given the same amount of run time on $N_{\text{CPU}} = 672$, and the other parameters are $J_{\text{max}} = 8$, $C_\varepsilon = 10^{-3}$, $C_0 = 20$ and $C_\eta = 1.65 \cdot 10^{-4}$.

Figure 8A shows the CPU cost t_{CPU} per grid point and time step. For smaller B_s , the cost increases because the overhead due to adaptivity becomes larger. Larger B_s reduces the cost per point because of the increased data regularity. It is important to compare the performance to other existing codes, therefore the computational cost for the spectral code FLUSI [32] is also shown. We choose this code because we can simulate exactly the same bumblebee setup with a completely different approach. In this simulation, the resolution is 2048^3 points and $N_{\text{CPU}} = 1152$. The comparably low N_{CPU} ensures best possible performance for the FLUSI code. By comparison, the performance of our new WABBIT code approaches that of the FLUSI code for larger B_s , which demonstrates that the additional overhead due to adaptivity is successfully mitigated by the block based data structure. Because of the full grid in the FLUSI case, the total cost is much more elevated, but on the other hand it relies on highly optimized FFT libraries. The similar performance per grid point and time step is thus a strong indicator for competitive performance of the WABBIT code.

For the WABBIT simulations, Fig. 8C shows the total number of points on the grid, averaged over the time span all simulations computed. It can be observed that as the computational cost per point decreases, the total number of points increases. Both influences combined yield Fig. 8B, which shows the total cost per simulation time unit. It presents a minimum for an intermediate value of B_s , where a compromise between sparsity and data regularity is made. We therefore choose $B_s = 23$, but we also note that any value between 15 and 30 would have resulted in near-optimal performance.

Figure 8D shows the fraction of CPU time spent on refinement, evolution and coarsening, which sum to 100%. Coarsening becomes cheaper with increasing B_s , while the relative cost for refinement is constant. The portion spent on the actual solution of the PDE (time evolution) increases with B_s , but even the lowest value is above 70%. We further show the relative time required for ghost node synchronization, which is done in all three of refinement, time evolution and coarsening. The synchronization is the crucial part for the parallelization, and it decreases, as expected, with increasing B_s . The performance data is machine-dependent, but the trends will be the same on other machines, thus this study gives a guideline how to choose B_s to obtain near-optimal performance.

Finally, we already discussed that parallelization of a dynamical grid is fundamentally different from static grids, because the work load per CPU is not constant. It is therefore important to verify that the performance remains indeed constant over a large range of blocks per CPU, N_b/N_{CPU} , as shown in Fig. 9. The data for this figure is accumulated from several simulations with N_{CPU} ranging from 672 to 5520. For $N_b/N_{\text{CPU}} > 50$, the performance is nearly constant, while it drops for smaller values. We therefore check periodically if $N_b/N_{\text{CPU}} > 50$ is satisfied and decrease the number of processes if it is not.

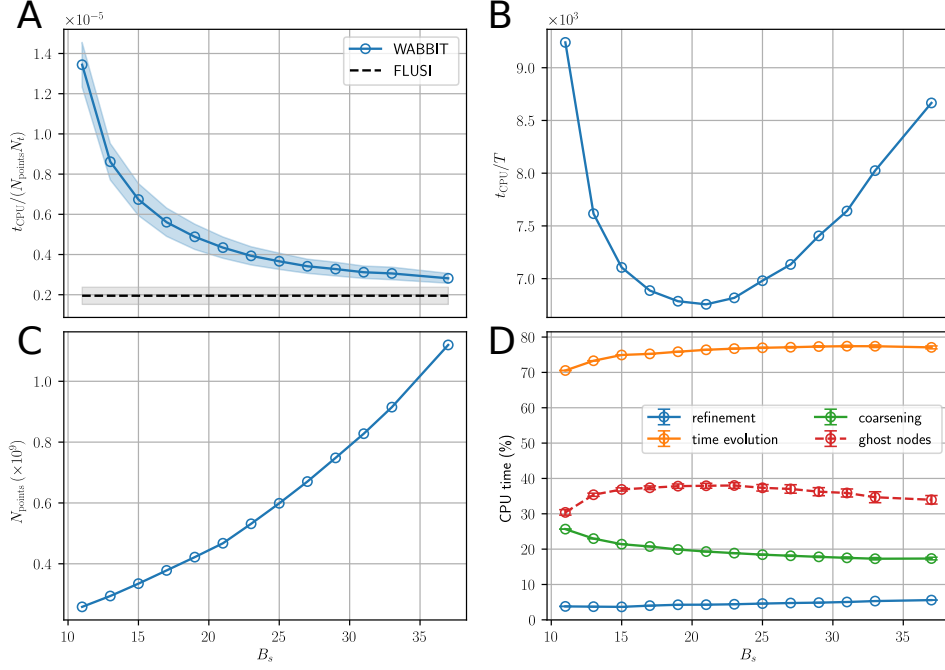


FIGURE 8. Bumblebee simulations, performance as a function of the block size B_s . A: CPU cost per grid point per time step. For comparison, the cost of the FLUSI code is included as well. Note only one simulation is shown, which does not depend on B_s . Shaded areas correspond to mean ± 1 s.d. B: total cost of simulation in CPUh per simulation time unit. C: Grid density $N_{\text{points}} = N_b(B_s - 1)^3$. D: fraction of time spend on grid refinement, time evolution and coarsening (=100%), as well as ghost node synchronization via MPI. All results are obtained with CDF 4/0 wavelets.

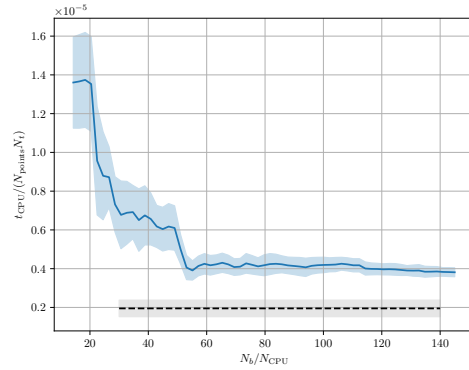


FIGURE 9. Bumblebee simulations, computational cost as a function of the number of blocks per CPU. Data for this figure is accumulated simulations with $672 \leq N_{\text{CPU}} \leq 5520$. For comparison, the cost of the FLUSI code is included as well. Note only one FLUSI simulation is shown, where the actual parallelization is constant. Shaded areas correspond to mean ± 1 s.d.

9. Conclusions. This article presents a novel framework for the wavelet-based adaptive simulations of turbulent flows in complex, time-dependent geometries on massively parallel computers. It is open-source in order to maximize its utility for the scientific community. The physical model is based on the original combination of artificial compressibility and volume penalization, which allows for an efficient implementation on fully adaptive grids, yielding both memory- and CPU time compression. Through numerical estimations and a series of validation cases, we discussed how the parameters for this model have to be chosen in order to reduce all occurring errors simultaneously while maintaining computational efficiency. Our implementation is based on block-structured grids, and the performance data illustrated how the size of these blocks is chosen to yield maximum efficiency. We furthermore showed that the performance per grid point and time step is very close to that of the Fourier pseudospectral code FLUSI. Because this spectral code relies on the fast Fourier transform, a task for which highly tuned libraries are used, we can conclude that our framework offers excellent performance and can indeed translate the sparsity of the grid into CPU time savings.

REFERENCES

- [1] S. Abhyankar, J. Brown, E. M Constantinescu, D. Ghosh, B. F. Smith, and H. Zhang. Petsc/ts: A modern scalable ode/dae solver library. *arXiv preprint arXiv:1806.01437*, 2018.
- [2] P. Angot, C. Bruneau, and P. Fabrie. A penalization method to take into account obstacles in incompressible viscous flows. *Numer. Math.*, 81:497–520, 1999.
- [3] E. Arquis and J.-P. Caltagirone. Sur les conditions hydrodynamiques au voisinage d’une interface milieu fluide milieu poreux: application à la convection naturelle. *C. R. Acad. Sci. Paris, Sér. II*, 299, 1984.
- [4] R. Becker and R. Rannacher. *An optimal control approach to a-posteriori error estimation*, pages 1–102. Cambridge University Press, Cambridge, 2001.
- [5] M. Berger and P. Colella. Local adaptive mesh refinement for shock hydrodynamics. *J. Comput. Phys.*, 82:64–84, 1988.
- [6] M. Berger and J. Oliger. Adaptive mesh refinement for hyperbolic partial differential equations. *J. Comput. Phys.*, 53:484–512, 1984.
- [7] A. Brandt. Multilevel adaptive solutions to boundary value problems. *Math. Comp.*, 31:333–390, 1977.
- [8] C. Burstedde, L. C. Wilcox, and O. Ghattas. **p4est**: Scalable algorithms for parallel adaptive mesh refinement on forests of octrees. *SIAM Journal on Scientific Computing*, 33(3):1103–1133, 2011.
- [9] A.J. Chorin. A numerical method for solving incompressible viscous flow problems. *J. Comput. Phys.*, 2:12–26, 1967.
- [10] A. Cohen. *Wavelet methods in numerical analysis*, volume VII of *Handbook of Numerical Analysis*. Elsevier, Amsterdam, 2000.
- [11] A. Cohen, W. Dahmen, and R. DeVore. Adaptive wavelet methods for elliptic operator equations – convergence rates. *Math. Comp.*, 70:27–75, 1998.
- [12] A. Cohen, I. Daubechies, and J. C. Feauveau. Biorthogonal bases of compactly supported wavelets. *Comm. Pure and Appl. Math.*, 45:485–560, 1992.
- [13] A. Cohen, N. Dyn, S. M. Kaber, and M. Postel. Multiresolution schemes on triangles for scalar conservation laws. *J. Comp. Phys.*, 161:264–286, 2000.
- [14] I. Daubechies. Orthonormal bases of compactly supported wavelets. *Comm. Pure and Appl. Math.*, 41(7):909–996, 1988.
- [15] R. Deiterding. *Parallel Adaptive Simulation of Multi-dimensional Detonation Structures*. PhD thesis, Brandenburgische Technische Universität Cottbus, 2003.
- [16] R. Deiterding. Construction and application of an amr algorithm for distributed memory computers. In Tomasz Plewa, Timur Linde, and V. Gregory Weirs, editors, *Adaptive Mesh Refinement - Theory and Applications*, pages 361–372, Berlin, Heidelberg, 2005. Springer Berlin Heidelberg.
- [17] R. Deiterding, M. Domingues, S. Gomes, O. Roussel, and K. Schneider. Adaptive multiresolution or adaptive mesh refinement? A case study for 2D Euler equations. *ESAIM: Proceedings*, 29:28–42, 2009.

- [18] R. Deiterding, M. Domingues, S. Gomes, O. Roussel, and K. Schneider. Comparison of adaptive multiresolution and adaptive mesh refinement applied to simulations of the compressible euler equations. *SIAM J. Sci. Comput.*, 38(5):S173–S193, 2016.
- [19] G. Deslauriers and S. Dubuc. Interpolation dyadique, 1987.
- [20] G. Deslauriers and S. Dubuc. Symmetric iterative interpolation processes. *Constr. Approx.*, 5(1):49, 1989.
- [21] R. A. DeVore. Nonlinear approximation. *Acta Numerica*, 7:51–150, 1998.
- [22] E. Dilek, B. Erzincanli, and M. Sahin. The numerical investigation of lagrangian and eulerian coherent structures for the near wake structure of a hovering drosophila. *Theoretical and Computational Fluid Dynamics*, Apr 2019.
- [23] M. Domingues, S. Gomes, O. Roussel, and K. Schneider. Adaptive multiresolution methods. *ESAIM: Proceedings*, 34:1–96, 2011.
- [24] M. Domingues, S. M. Gomes, and L. M. A. Díaz. Adaptive wavelet representation and differentiation on block-structured grids. *Appl. Num. Math.*, 47:421–437, 2003.
- [25] D L Donoho. Interpolating wavelet transforms. *Preprint, Department of Statistics, Stanford University*, 2(3):1–54, 1992.
- [26] D. L. Donoho and J. M. Johnstone. Ideal spatial adaptation by wavelet shrinkage. *biometrika*, 81(3):425–455, 1994.
- [27] T. Engels, D. Kolomenskiy, K. Schneider, M. Farge, F.-O. Lehmann, and J. Sesterhenn. Helical vortices generated by flapping wings of bumblebees. *Fluid Dyn. Res.*, 50:011419, 2018.
- [28] T. Engels, D. Kolomenskiy, K. Schneider, M. Farge, F.-O. Lehmann, and J. Sesterhenn. Impact of turbulence on flying insects in tethered and free flight: High-resolution numerical experiments. *Phys. Rev. Fluids*, 4:013103, Jan 2019.
- [29] T. Engels, D. Kolomenskiy, K. Schneider, F.-O. Lehmann, and J. Sesterhenn. Bumblebee flight in heavy turbulence. *Phys. Rev. Lett.*, 116:028103, 2016.
- [30] T. Engels, D. Kolomenskiy, K. Schneider, and J. Sesterhenn. Two-dimensional simulation of the fluttering instability using a pseudospectral method with volume penalization. *Computers & Structures*, 122:101–112, 2012.
- [31] T. Engels, D. Kolomenskiy, K. Schneider, and J. Sesterhenn. Numerical simulation of fluid-structure interaction with the volume penalization method. *J. Comput. Phys.*, 281:96–115, 2015.
- [32] T. Engels, D. Kolomenskiy, K. Schneider, and J. Sesterhenn. FluSI: A novel parallel simulation tool for flapping insect flight using a Fourier method with volume penalization. *SIAM J. Sci. Comput.*, 38(5):S3–S24, 2016.
- [33] M. Farge, K. Schneider, and N. Kevlahan. Non-Gaussianity and Coherent Vortex Simulation for two-dimensional turbulence using an adaptive orthonormal wavelet basis. *Phys. Fluids*, 11:2187–2201, 1999.
- [34] I. Gargantini. An effective way to represent quadrtrees. *Communications of the ACM*, 25(12):905–910, 1982.
- [35] I. Gargantini. Linear octrees for fast processing of three-dimensional objects. *Computer graphics and Image processing*, 20(4):365–374, 1982.
- [36] A George, LC Huang, W-P Tang, and YD Wu. Numerical simulation of unsteady incompressible flow ($Re \leq 9500$) on the curvilinear half-staggered mesh. *SIAM J. Sci. Comput.*, 21(6):2331–2351, 2000.
- [37] A. Grossmann and J. Morlet. Decomposition of Hardy functions into square integrable wavelets of constant shape. *SIAM J. Math. Anal.*, 15:723–736, 1984.
- [38] J. Guermond and P. Mineev. High-order time stepping for the incompressible Navier–Stokes equations. *SIAM Journal on Scientific Computing*, 37(6):A2656–A2681, 2015.
- [39] A. Harten. Discrete multi-resolution analysis and generalized wavelets. *Appl. Numer. Anal.*, 12:153–192, 1993.
- [40] A. Harten. Multiresolution algorithms for the numerical solution of hyperbolic conservation laws. *Comm. Pure Appl. Math.*, 48:1305–1342, 1995.
- [41] A. Harten. Multiresolution representation of data: a general framework. *SIAM J. Numer. Anal.*, 33:385–394, 1996.
- [42] D. Hilbert. über die stetige Abbildung einer Linie auf ein Flächenstück. *Mathematische Annalen*, 38:459–460, 1891.
- [43] M. Holmström. Solving hyperbolic PDEs using interpolating wavelets. *SIAM J. Sci. Comput.*, 21(2):405–420, 1999.
- [44] N. Kevlahan and M. Farge. Vorticity filaments in two-dimensional turbulence: Creation, stability and effect. *J. Fluid Mech.*, 346:49–76, 1997.
- [45] N. Kevlahan and O. Vasilyev. An adaptive wavelet collocation method for fluid–structure interaction at high Reynolds numbers. *SIAM J. Sci. Comput.*, 26(6):1894–1915, 2005.

- [46] D. Kolomenskiy, J.-C. Nave, and K. Schneider. Adaptive gradient-augmented level set method with multiresolution error estimation. *J. Sci. Comput.*, 66:116–140, 2016.
- [47] D. Kolomenskiy and K. Schneider. A Fourier spectral method for the Navier-Stokes equations with volume penalization for moving solid obstacles. *J. Comput. Phys.*, 228:5687–5709, 2009.
- [48] P. Koumoutsakos and A. Leonard. High-resolution simulations of the flow around an impulsively started cylinder using vortex methods. *J. Fluid Mech.*, 296:1–38, 1995.
- [49] J. Liandrat and P. Tchamitchian. Resolution of the 1d regularized Burgers equation using a spatial wavelet approximation. Technical report, 1990.
- [50] S. Mallat. Multiresolution approximation and orthonormal wavelet basis of $l_2(\mathbb{R})$. *Trans. Am. Math. Soc.*, 315:69–87, 1989.
- [51] S. Mallat. *A Wavelet Tour of Signal Processing The Sparse Way*. Academic Press, 3rd edition, 2009.
- [52] R. Mittal and G. Iaccarino. Immersed boundary methods. *Annu. Rev. Fluid Mech.*, 37:239–261, 2005.
- [53] S. Müller. *Adaptive multiscale schemes for conservation laws*, volume 27 of *Lectures Notes in Computational Science and Engineering*. Springer, Heidelberg, 2003.
- [54] R. Nguyen van yen, D. Kolomenskiy, and K. Schneider. Approximation of the Laplace and Stokes operators with Dirichlet boundary conditions through volume penalization: A spectral viewpoint. *Numer. Math.*, 128:301–338, 2014.
- [55] T. Ohwada and P. Asinari. Artificial compressibility method revisited: Asymptotic numerical method for incompressible Navier–Stokes equations. *J. Comp. Phys.*, 229:1698–1723, 2010.
- [56] C. S. Peskin. Numerical analysis of blood flow in the heart. *J. Comput. Phys.*, 25:220–252, 1977.
- [57] C. S. Peskin. The immersed boundary method. *Acta Numerica*, 11:479–517, 2002.
- [58] D. Rossinelli, C. Conti, and P. Koumoutsakos. Mesh-particle interpolations on graphics processing units and multicore central processing units. *Philosophical Transactions of the Royal Society A: Mathematical, Physical and Engineering Sciences*, 369(1944):2164–2175, may 2011.
- [59] O. Roussel and K. Schneider. Coherent Vortex Simulation of weakly compressible turbulent mixing layers using adaptive multiresolution methods. *J. Comput. Phys.*, 229:2267–2286, 2010.
- [60] O. Roussel, K. Schneider, A. Tsigulin, and H. Bockhorn. A conservative fully adaptive multiresolution algorithm for parabolic PDEs. *J. Comput. Phys.*, 188:493–523, 2003.
- [61] K. Schneider. Immersed boundary methods for numerical simulation of confined fluid and plasma turbulence in complex geometries: a review. *J. Plasma Phys.*, 81:435810601, 2015.
- [62] K. Schneider and O. Vasilyev. Wavelet methods in computational fluid dynamics. *Annu. Rev. Fluid Mech.*, 42:473–503, 2010.
- [63] F. Schornbaum and U. Rüde. Extreme-scale block-structured adaptive mesh refinement. *SIAM Journal on Scientific Computing*, 40(3):C358–C387, 2018.
- [64] B. Seibold, R. Rosales, and J.C. Nave. Jet schemes for advection problems. *Discrete Contin. Dyn. Syst. Ser. B*, 17(4):1229–1259, 2012.
- [65] K. Suzuki, K. Minami, and T. Inamuro. Lift and thrust generation by a butterfly-like flapping wing-body model: immersed boundary-lattice Boltzmann simulations. *J. Fluid Mech.*, 767:659–695, 2015.
- [66] W. Sweldens. The lifting scheme: A construction of second generation wavelets. *SIAM J. Math. Anal.*, 29(2):511–546, 1989.
- [67] W. Sweldens and P. Schröder. Building your own wavelets at home. *Wavelets in Computer Graphics*, 1997.
- [68] W. Sweldens and P. Schröder. *Building your own wavelets at home*, pages 72–107. Springer Berlin Heidelberg, Berlin, Heidelberg, 2000.
- [69] C. K.W. Tam and J. C. Webb. Dispersion-relation-preserving finite difference schemes for computational acoustics. *Journal of Computational Physics*, 107(2):262–281, 1993.
- [70] G. Zumbusch. *Parallel multilevel methods: adaptive mesh refinement and loadbalancing*. Advances in Numerical Mathematics. Springer, 2003.

Appendix A. Approximation for first derivatives. In the present work, we use the optimized fourth order scheme proposed by Tam and Webb [69] for first derivatives. It is built on the idea of combining a fourth- and a sixth order approximation using standard finite differences, yielding

$$(\partial_x u)_i \approx \Delta x^{-1} \left(\sum_{j=-n}^n \left(\gamma a_j^{(4\text{th})} + (1 - \gamma) a_j^{(6\text{th})} \right) u_{i+j} \right)$$

where $a_j^{(4\text{th})}$ and $a_j^{(6\text{th})}$ are classical, central finite differences. The combination provides a degree of freedom γ , which is then used to optimize the modified wavenumber. The resulting stencil is

$$a_j^{(\text{TW})} = -a_{-j}^{(\text{TW})} = \{-0.02651995, 0.18941314, -0.79926643, 0\}, \quad (-3 \leq j \leq 0).$$

Appendix B. Filter Coefficients for CDF wavelets. The filter coefficients for the biorthogonal wavelets used in this work (CDF 4/0 and CDF 4/4) are given in Table 1.

CDF4/0				CDF4/4			
\tilde{h}	\tilde{g}	h	g	\tilde{h}	\tilde{g}	h	g
i							
-7							$-\frac{1}{256}$
-6				$-\frac{1}{256}$			0
-5				0			$\frac{9}{128}$
-4				$\frac{9}{128}$			$\frac{1}{16}$
-3		$-\frac{1}{16}$		$-\frac{1}{16}$		$-\frac{1}{16}$	$-\frac{63}{256}$
-2	$\frac{1}{16}$	0		$-\frac{63}{256}$	$\frac{1}{16}$	0	$-\frac{9}{16}$
-1	0	$\frac{9}{16}$		$\frac{9}{16}$	0	$\frac{9}{16}$	$\frac{87}{64}$
0	1	$-\frac{9}{16}$	1	$\frac{87}{64}$	$-\frac{9}{16}$	1	$-\frac{9}{16}$
1		1	$\frac{9}{16}$	1	$\frac{9}{16}$	1	$-\frac{63}{256}$
2		$-\frac{9}{16}$	0	$-\frac{63}{256}$	$-\frac{9}{16}$	0	$\frac{1}{16}$
3		0	$-\frac{1}{16}$	$-\frac{1}{16}$	0	$-\frac{1}{16}$	$\frac{9}{128}$
4		$\frac{1}{16}$		$\frac{9}{128}$	$\frac{1}{16}$		0
5				0			$-\frac{1}{256}$
6				$-\frac{1}{256}$			

TABLE 1
Filter coefficients for the CDF4/0 and CDF4/4 interpolating biorthogonal wavelets.

Appendix C. Validation for a linear PDE. As an additional validation case, we now consider a benchmarking problem for the linear transport equation, $\partial_t \theta + \underline{u} \cdot \nabla \theta = 0$, where $\theta(x, y, t)$ is a scalar and $0 \leq x, y < 1$. The domain is periodic in

two-dimensional space. The initial condition is a Gaussian blob,

$$\theta(x, y, 0) = e^{-((x-c)^2 + (y-d)^2)/\beta}$$

where we set $c = 0.5$, $d = 0.75$ and $\beta = 0.01$. The time-dependent velocity field is given by

$$(C.1) \quad \underline{u}(\underline{x}, t) = \cos\left(\frac{\pi t}{T_a}\right) \begin{pmatrix} \sin^2(\pi x) \sin(2\pi y) \\ \sin^2(\pi y) (-\sin(2\pi x)) \end{pmatrix}$$

and swirls the initial condition, but reverses to the initial state at $t = T_a$. Its divergence is $\nabla \cdot \underline{u} = 0$. The swirling motion produces increasingly fine structures until $t = T_a/2$, where T_a controls also the size of structures. The larger T_a , the more challenging is the test. In our simulations, we set $T_a = 5.0$.

As for the discretization, the method is the same as the one used to solve the artificial compressibility equations. Spatial derivatives are discretized with a 4th-order, central finite-difference scheme with optimized modified wavenumbers [69] and we use a 4th-order Runge–Kutta time integration. Interpolation for the refinement operator is also 4th order and we use a block size of $B_s = 33$.

In the original design of the test [46, 64], the computations are performed until $t = T_a$, and the error is evaluated with respect to the initial condition. The temporal symmetry of the swirl field can however result in error cancellation, provided the discretization is conservative. Dispersion errors can cancel out. We therefore run the simulation only until the point of maximum distortion ($t = T_a/2$), and compare with a spectral reference solution.

Figure 10A illustrates θ at the initial time, $t = 0$, and the instant of maximal distortion at $t = T_a/2$. At $t = T_a/2$ the grid is strongly refined in regions of fine structures, while the remaining part of the domain features a coarser resolution, *e.g.*, in the center of the domain.

Figure 10B illustrates the relative error $\|\theta - \theta_{\text{spectral}}\|_{\infty} / \|\theta_{\text{spectral}}\|_{\infty}$ as a function of the multiresolution threshold C_{ε} and for different J_{max} . For the computation of the error, all adaptive grids are first interpolated to an equidistant grid with their given J_{max} , then the norms are computed. The error first decays, as expected, almost linearly in C_{ε} , the precise slope being 0.93 (black dashed line). Once a threshold $C_{\varepsilon, \text{opt}}(J_{\text{max}})$ is reached, the discretization error saturates and further reducing C_{ε} does no longer increase the overall precision. The value of $C_{\varepsilon, \text{opt}}$ can be estimated as the intersection between the constant discretization error and the linear slope in C_{ε} .

Figure 10C visualizes the data for the smallest C_{ε} considered for each J_{max} , as well as the optimum value $C_{\varepsilon, \text{opt}}$, as a function of the smallest grid spacing $\Delta x = L2^{-J_{\text{max}}}/(B_s - 1)$. For this linear problem, we find the convergence to be very close to Δx^4 . We can therefore conclude that our framework preserves the convergence rates of the underlying space- and time discretization on dynamically adapted grids. Tracing $C_{\varepsilon, \text{opt}}$ as a function of Δx is shown in Fig. 10D.

Appendix D. Non-reflecting boundary conditions using sponges. At the outflow boundary of the computational domain, we impose non-reflecting boundary conditions using a sponge technique. The outflow removes two physically distinct phenomena: on the one hand, vortical structures not yet dissipated, and artificial sound waves on the other. The artificial sound waves transport flow divergence created at the fluid–solid interface and due to the nonlinear term. It is possible to implement such conditions based on characteristics, but for simplicity and consistency with the

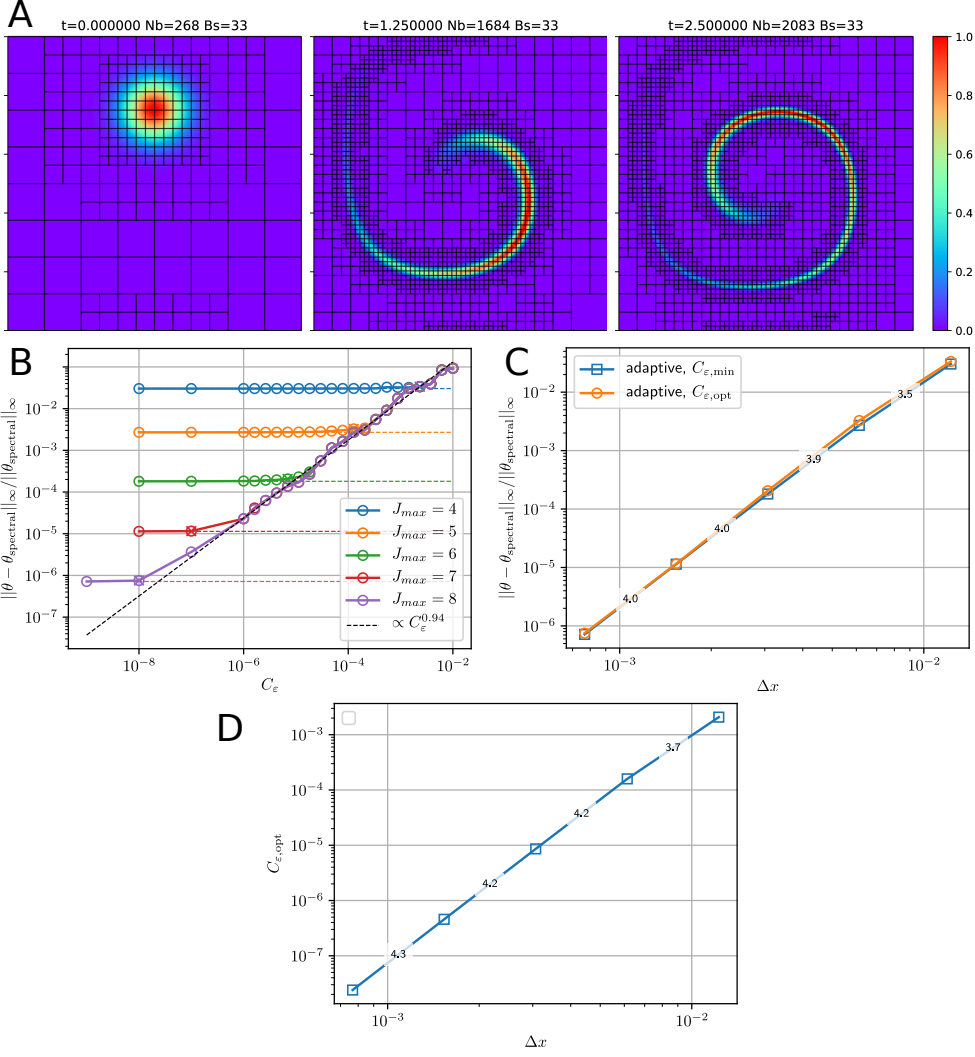


FIGURE 10. *Swirl test.* A: Snapshots of the scalar field θ at $t = 0$, $T_a/4$ and $T_a/2$, from left to right. In this simulation, $J_{\text{max}} = 7$ and $C_{\epsilon} = 10^{-8}$. B: error $\|\theta - \theta_{\text{spectral}}\|_{\infty} / \|\theta_{\text{spectral}}\|_{\infty}$ as a function of the multiresolution threshold C_{ϵ} and for different J_{max} . C: The convergence for the smallest value of C_{ϵ} as a function of the finest grid spacing Δx . D: Optimal value of C_{ϵ} as a function of the minimal spacing Δx .

treatment of the obstacles, we use the volume penalization method to include non-reflecting sponges. We can conveniently discuss the choice of parameters for sponges using a simple, one-dimensional model. In the acoustic regime, we can neglect the nonlinear and diffusion terms, and we also remove the obstacle penalization term, yielding

$$\begin{aligned}\partial_t u &= -\partial_x p - \frac{\chi_{\text{sp}}}{C_{\text{sp}}} u \\ \partial_t p &= -\partial_x u - \frac{\chi_{\text{sp}}}{C_{\text{sp}}} p,\end{aligned}$$

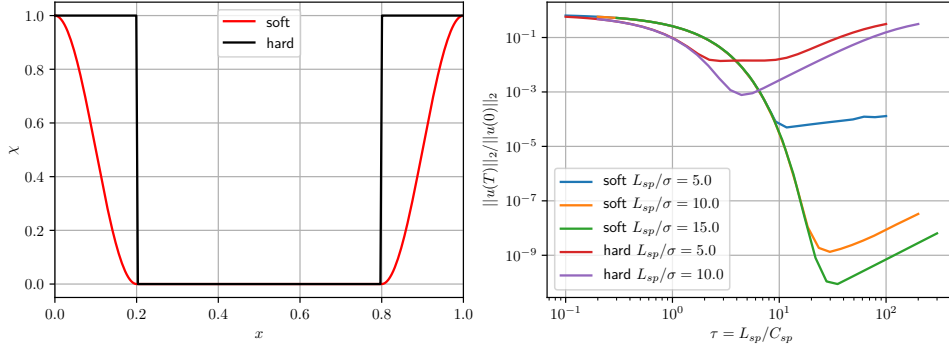


FIGURE 11. *Left: Hard and smooth χ functions, here with $L_{sp} = 0.2$. The red function is cos-shaped. Right: sponge error, computed as L^2 norm of residual velocity at $t = T$. Because the exact solution at is zero, we use $\|u(t=0)\|_2$ as normalization.*

where we further normalize $C_0 = 1$ without loss of generality. The reference state is $u_\infty = p_\infty = 0$. Consider a periodic domain of length L and the initial condition

$$\begin{aligned} u(x, t = 0) &= \exp(-(x - L/2)^2 / \sigma^2) \\ p(x, t = 0) &= 0. \end{aligned}$$

This initial condition results in two artificial sound waves with characteristic size σ traveling left and right. The waves do not decay in a 1D setting, unlike in higher dimensions, making the 1D problem the most sensitive to non-reflecting boundary conditions. In 3D, the waves decay as R^{-2} , where R is the distance to the source. Provided a sufficiently large domain, pseudoacoustic waves thus are already significantly weakened when reaching the sponge layer.

The size of the sponge layer should be larger than the waves it is supposed to absorb – the important ratio is thus L_{sp}/σ . The second relevant parameter is the time spent in the sponge layer, relative to the relaxation time C_{sp} . We call this parameter $\tau = L_{sp}/(C_0 C_{sp})$. The third relevant parameter is the shape χ_{sp} of the sponge layer, for which we can use either a discontinuous or smoothed function as shown in Fig. 11 (left).

Depending of the choice of parameters, one of two things can happen: the damping is too weak, and the wave is not completely removed from the domain (it re-enters on the opposite side). The damping can also be too strong, in which case the sponge term deteriorates the regularity of the solution and spurious reflections occur. We run the simulations until $T = 3L/4$; the artificial wave reaches the sponge around $T_0 = (L - L_{sp})/2$. The exact solution at $t = T$ is $u = p = 0$. Figure 11 (right) shows the normalized residual velocity at the final time T for hard and soft mask function and different L_{sp}/σ , as a function of τ . The curves coincide for small τ , which indicates that L_{sp}/σ and τ are indeed the relevant parameters. Thicker sponges allow setting larger values of τ , which reduces reflections. However, a significant improvement of the soft mask function over the discontinuous one is observed, and almost perfect cancellation of waves is observed for the largest L_{sp}/σ . From this data, we conclude that $L_{sp}/\sigma > 5$ and $\tau > 10$ minimize reflections. Because sponges are usually set much larger than $L_{sp}/\sigma = 5$, because of vortical structures, we recommend setting $\tau = 20$ in the main text. Note that in practice, simulations are performed in 3D and the sensitivity to the sponge is then significantly reduced.